Mon. Not. R. Astron. Soc. **000**, 000–000 (0000) Printed 5 February 2008 (MN LATEX style file v2.2)

Towards an understanding of the Of?p star HD 191612: optical spectroscopy

Ian D. Howarth,[1]* Nolan R. Walborn,[2] Danny J. Lennon,[3] Joachim Puls,[4] Yaël Nazé,[5] K. Annuk,[6] I. Antokhin,[7] D. Bohlender,[8] H. Bond,[2] J.-F. Donati,[9] L. Georgiev,[10] D. Gies,[11] D. Harmer,[12] A. Herrero,[13] I. Kolka,[6] D. McDavid,[14] T. Morel,[15] I. Negueruela,[16] G. Rauw,[5] P. Reig[17]

[1] *Dept. of Physics and Astronomy, University College London, Gower Street, London WC1E 6BT, UK*
[2] *Space Telescope Science Institute, 3700 San Martin Drive, Baltimore, MD 21218, USA*
[3] *The Isaac Newton Group of Telescopes, Apartado de Correos 321, 38700 Santa Cruz de La Palma, Canary Islands, Spain*
[4] *Universitäts-Sternwarte München, Scheinerstr. 1, 81679 München, Germany*
[5] *FNRS Institut d'Astrophysique et de Géophysique, Université de Liège, Bât. B5c, Allée du VI Août 17, B-4000 Liège, Belgium*
[6] *Tartu Observatory, 61602 Tõravere, Estonia*
[7] *Sternberg Astronomical Institute, Moscow University, Universitetskij Prospect 13, Moscow 119992, Russia*
[8] *National Research Council of Canada, Herzberg Institute of Astrophysics, 5071 West Saanich Road, Victoria, BC V9E 2E7, Canada*
[9] *Laboratoire d'Astrophysique, Observatoire Midi-Pyrénées, 14 Av. E. Belin, F-31400 Toulouse, France*
[10] *Instituto de Astronomía, UNAM, Apartado Postal 70-254, CD Universitaria, CP 04510 México DF, Mexico*
[11] *Department of Physics and Astronomy, Georgia State University, P.O. Box 4106, Atlanta, GA 30302-4106, USA*
[12] *Kitt Peak National Observatory, NOAO, P.O. Box 26732, Tucson, AZ 85719, USA*
[13] *Instituto de Astrofísica de Canarias, 38200 La Laguna, Tenerife, Spain*
[14] *Department of Astronomy, University of Virginia, P.O. Box 400325, Charlottesville, VA 22904-4325, USA*
[15] *Katholieke Universiteit Leuven, Departement Natuurkunde en Sterrenkunde, Instituut voor Sterrenkunde, Celestijnenlaan 200D, B-3001 Leuven, Belg*
[16] *Departamento de Fsica, Ingeniería de Sistemas y Teoría de la Señal, Escuela Politécnica Superior, Universidad de Alicante, Ap. 99, 03080 Alicante, Spain*
[17] *IESL, Foundation for Research and Technology, 71110 Heraklion, Greece*

arXiv:0707.0594v1 [astro-ph] 4 Jul 2007

Dates to be inserted

ABSTRACT

We present extensive optical spectroscopy of the early-type magnetic star HD 191612 (O6.5f?pe–O8fp). The Balmer and He I lines show strongly variable emission which is highly reproducible on a well-determined 538-d period. Metal lines and He II absorptions (including many selective emission lines but excluding He II λ4686Å emission) are essentially constant in line strength, but are variable in velocity, establishing a double-lined binary orbit with $P_{\rm orb} = 1542$d, $e = 0.45$. We conduct a model-atmosphere analysis of the primary, and find that the system is consistent with a ∼O8 giant with a ∼B1 main-sequence secondary. Since the periodic 538-d changes are unrelated to orbital motion, rotational modulation of a magnetically constrained plasma is strongly favoured as the most likely underlying 'clock'. An upper limit on the equatorial rotation is consistent with this hypothesis, but is too weak to provide a strong constraint.

1 INTRODUCTION

Peculiarities in the spectrum of the early-type star HD 191612 were first noted by Walborn (1973); it remains one of only three known Galactic examples of the Of?p class,[1] this designation indicating C III λ4650 in emission with comparable strength to N III λ4640. Renewed interest followed the discovery of recurrent spectral variability between spectral types O6–O7 and O8 (with correlated changes in the unusual emission-line features; Walborn et al. 2003), which Walborn et al. (2004) showed to be consistent with a ∼540-d period identified in *Hipparcos* photometry (Koen & Eyer 2002; Nazé 2004).

From timescale arguments, Walborn et al. (2004) suggested that the 'clock' underlying the variability was most probably a binary orbit. New light was cast on this issue by Donati et al. (2006a), who found HD 191612 to be only the second O-type star known to possess a magnetic field.[2] Although their observations sampled only a single epoch, they were none the less able to estimate a polar field strength of

[1] The others are HD 108 & HD 148937; the SMC Of?p stars AzV 220 & 2dFS 936 were found subsequently (Walborn et al. 2000; Massey & Duffy 2001; Evans et al. 2004).

[2] The first was θ^1 Ori C; Donati et al. (2002).

∼1.5kG (from an observed line-of-sight field of ∼220G, by assuming a dipole field), and made the case for 538-d *rotational* modulation, arguing that the field itself could easily be responsible for the implied slow rotation (through magnetic braking).

Of observational necessity, the magnetic, rotational-modulation model is as yet poorly constrained, and the discussion of XMM-Newton spectroscopy by Nazé et al. (2007) emphasizes a number of discrepancies with the X-ray behaviour expected in the simplest version of this scenario. On the other hand, the alternative orbital model has not been subject to any strong tests (arguably, even a strict, coherent spectroscopic periodicity has yet to be demonstrated robustly). Here we present the results of an extensive campaign of optical spectroscopy, carried out in an attempt to shed light on these issues.

2 OBSERVATIONS

The major part of our campaign was conducted during the 2004 and 2005 observing seasons. Because of the ∼18-month variability timescale, scheduled observations at common-user facilities were generally impractical, and our observations were obtained through service programmes; by taking advantage of telescope time awarded to other scheduled programmes; and by exploiting the goodwill of colleagues. The main dataset, summarized in Table A1 (166 digital observations spanning 17 years), is therefore quite heterogeneous. None the less, the spectra can be conveniently characterized by wavelength range ('red', including Hα 6563Å; 'blue', generally including at least the ∼4400–4700Å region) and by resolution ('high', $R \gtrsim 4 \times 10^4$; 'intermediate', $R \gtrsim 4 \times 10^3$; and 'low'). With a few exceptions, the spectra are generally reasonably well exposed, with signal:noise ratios typically approaching ∼100.

All spectra have been put on a heliocentric velocity scale, and all the Hα spectra have been corrected for telluric absorption by division, in topocentric space, with an appropriately scaled and smoothed telluric 'map' constructed from high-quality, high-dispersion echelle spectra. (Because the telluric lines are unresolved, direct scaling in optical depth is impossible; we scaled in observed intensity, but checked that scaling in observed, pseudo-optical depth gives negligibly different results.)

3 THE 538-D PERIOD: Hα VARIABILITY

As already noted by Nazé et al. (2007), the spectral lines can, for the most part, be separated into two groups according to variability characteristics: the absorption lines of metals and of He II show, at most, small changes in line strength, while the hydrogen and He I lines show large equivalent-width changes. Hα shows the largest-amplitude variations of any spectral feature followed in our campaign, by a comfortable margin. This, and the rather extensive temporal coverage of the red-region spectra, mean that it is the most useful feature for investigating the periodicity of the spectroscopic variability.

Table 1. Hα variability: best-fit parameters for the arbitrary functional form described by eqtn 1.

W_0	2.51	±	0.18	Å
A	6.74		0.16	Å
P_α	537.6		0.4	d
t_0	JD 2,453,415.2		0.5	
σ_ϕ	0.177		0.005	
ϕ_0	0.337		0.005	

3.1 Ephemeris

Even casual inspection shows systematic variations in Hα that repeat on a period close to the ∼540-d timescale found in *Hipparcos* photometry (over only about 2 cycles). In order to quantify that period and its uncertainty, we fit an *ad hoc* analytical function to the equivalent-width measurements; we find that a truncated gaussian,

$$W_\lambda(\phi_\alpha) = W_0 - A \exp\left\{\frac{-\phi_\alpha^2}{2\sigma_\phi^2}\right\} \qquad -\phi_0 < \phi_\alpha < +\phi_0$$
$$= W_\lambda(\phi_0) \qquad \phi_0 \le \phi_\alpha \le 1 - \phi_0 \qquad (1)$$

gives a good match to the observations. Although this functional form is arbitrary, it does provide a useful characterization of the data; the best-fit parameters are listed in Table 1, and lead to the ephemeris

$$\phi_\alpha = (t - \text{JD } 2453415.2)/537.6\text{d} \qquad (2)$$

where phase zero corresponds to peak Hα emission.[3]

The phase-zero epoch is chosen to be close to the median date of the observations (to minimize the formal error on t_0), and so, because the density of observations has increased with time, many spectra were obtained at negative epochs. For such observations we use a logarithmic-like notation for phases, such that $\phi_\alpha = \overline{1}.23$ means phase +0.23 in cycle −1.

3.2 Hα Properties

Figure 1 shows the Hα equivalent-width measurements, which vary between +1.4 and −4.3Å, folded on the adopted ephemeris; it illustrates a number of noteworthy points:

(i) The Hα light-curve is remarkably symmetrical about phase zero.

(ii) There is a well-defined interval of apparent 'quiescence', lasting ∼ 0.3(= 1–2ϕ_0) of the period.

(iii) The behaviour is repeatable from the earliest quantitative data (1982),[4] supporting a truly periodic underlying 538-d 'clock'.

(iv) None the less, the Hα profiles are evidently not *strictly* repeatable; the standard deviation of W_λ measurements about the functional fit is only 0.16Å, but scrutiny

[3] This differs from the Walborn et al. (2004) ephemeris (which was tied to the less well determined minimum in the *Hipparcos* photometry) by half a cycle.

[4] We measured the equivalent width from a digitized version of the plot of Hα given by Peppel (1984), who observed on JD 2,445,211, 24 years before our last observation. We included this point in the fit of eqn. 1, but its exclusion makes no important changes to the ephemeris.

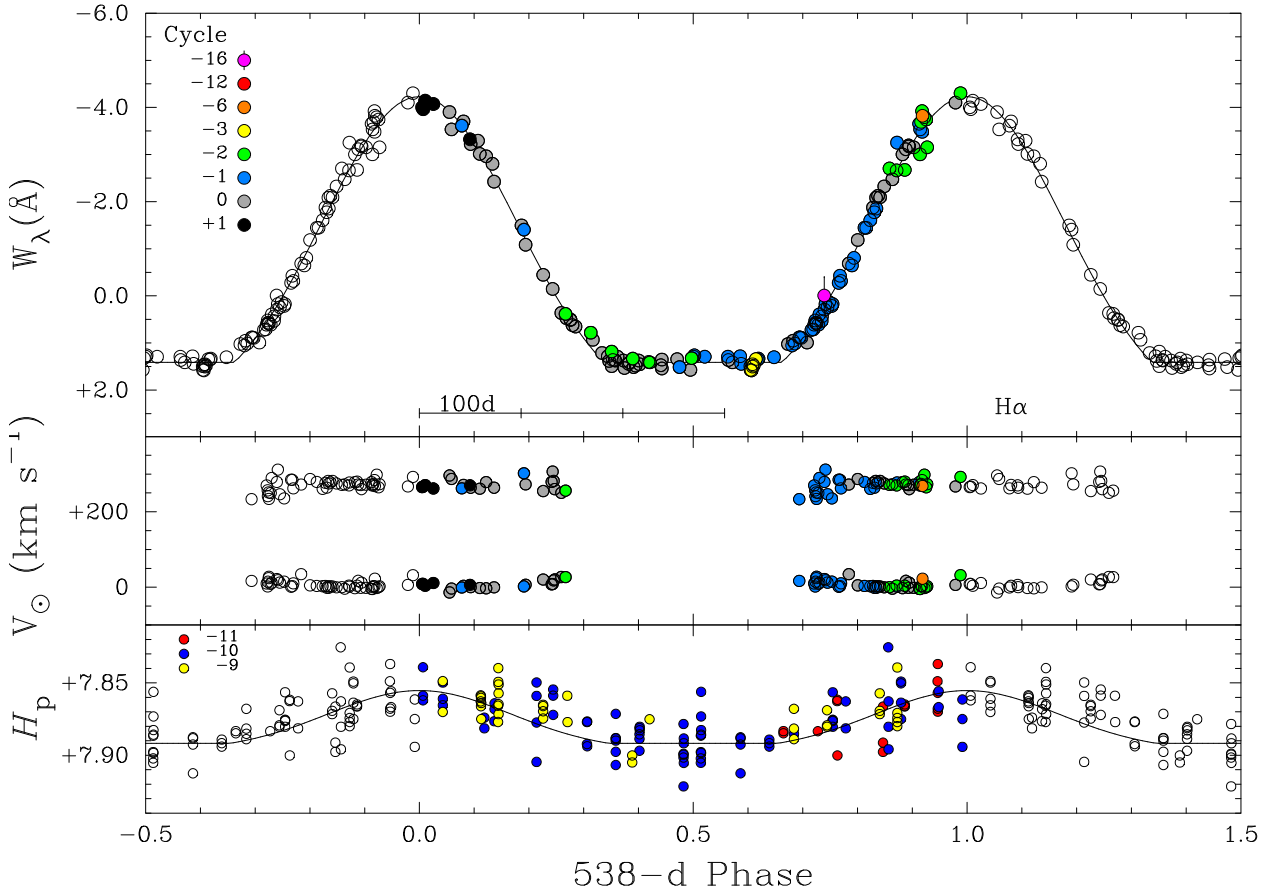

Figure 1. Hα measurements folded on the ephemeris of eqtn. 2, shown over two cycles. *Upper panel:* equivalent width (the solid line is the *ad hoc* functional fit, eqtn. 1, described in Section 3.1). *Middle panel:* FWHM (upper groups of points) and central velocity (lower) of excess emission. *Bottom panel:* the *Hipparcos* photometry (with a scaled, vertically shifted version of the Hα functional fit to guide the eye).

of the spectra shows that real, small-amplitude variability contributes to this dispersion at all sufficiently well-sampled phases, including quiescence, on timescales longer than a few days. We suspect that any O-type star observed as extensively and intensively as HD 191612 may show Hα 'jitter' at a similar level (cf., e.g., Kaper et al. 1997; Morel et al. 2004).

The Hα profile during quiescence is asymmetric and filled in by stellar-wind emission (Fig. 2). It is intermediate in appearance between the profiles of HD 36861 [λ Ori; O8 III((f)), pure absorption] and HD 175754 [O8 II((f)), P Cygni], although the closest matches among the spectra at our disposal are with HD 193514 [O7 Ib(f)] and HD 209975 [O9.5 Ib; fig. 2].[5] Thus while we have no exact match to the quiescent spectrum, the Hα profile in that state seems to be largely unremarkable, with no evidence of substantial excess emission relative to normal stars of broadly comparable spectral type.

At other phases, the line-profile morphology is P-Cygni-*like*, but the increase in emission is not necessarily associated with an increase in the global mass-loss rate (cf. Sec. 4.2). Phenomenologically, the changes in the appearance of the profile can be entirely accounted for by variable amounts of roughly gaussian emission superimposed on a constant, underlying quiescent-state spectrum (Fig. 2). We have characterized the mean velocity displacement and width of this excess emission by gaussian fits; results are incorporated in Fig. 1. Significant phase dependence is evident for neither mean velocity nor fwhm, which average +7 km s^{-1} and 271 km s^{-1}, respectively (standard deviations 10 and 16 km s^{-1}, commensurate with likely observational uncertainties); the width of the excess emission is much less than both the stellar-wind terminal velocity (Sec. 6.4), and the 'windy' Hα emission normally seen in luminous O stars.

Finally, although the Hα and *Hipparcos* light-curves are in phase (to within the errors), we note that the photometric variations are too large to result from excess line emission alone; most of the ∼3–4% flux change must arise from true continuum-level variations.

[5] We also examined the spectrum of HD 225160; surprisingly, this O8 Ib(f) star shows much stronger emission than the O7 and O9.5 Ib stars.

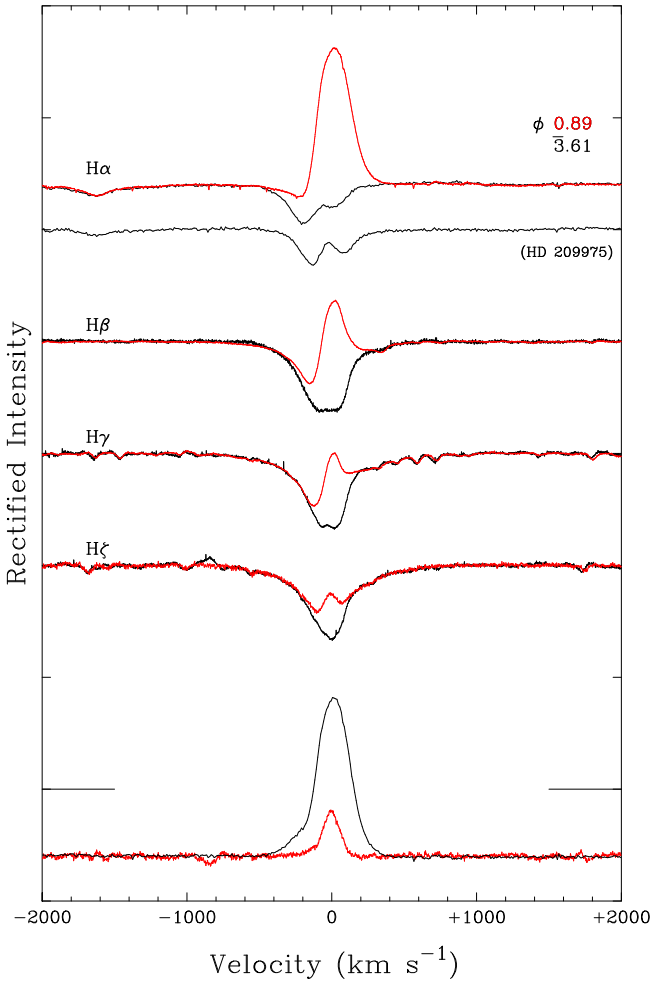

Figure 2. Balmer-line profiles for HD 191612 at quiescence ($\phi = \overline{3}.61$, in black) and near emission maximum ($\phi = 0.89$, red); tickmarks on the y axis are separated by half the continuum level. The Hα spectrum of HD 209975 is included to demonstrate that a near match to the minimum-state spectrum can be found among normal stars (see Section 3.2 for details). Difference spectra for Hα and Hζ are shown at the bottom of the plot. Velocities are heliocentric.

4 THE 538-D PERIOD: OTHER VARIABLE LINES

4.1 Balmer and He I lines

Other Balmer lines (to at least H10)[6] and the He I lines all show large variations, in both strength and velocity, which are reproducible on the 538-d period. He I 4471Å (Fig. 3) exemplifies the typical behaviour of the He I lines; most remain in absorption at all phases, although He I $\lambda\lambda$5876, 7065, 7281, as well as Hα and Hβ, show strong P-Cygni-like emission at maximum. While most lines are in absorption during quiescent phases (even Hα, as illustrated with other Balmer lines in Fig. 2), He I 6678Å is exceptional in retaining an emission core (Fig. 4).

[6] Paschen lines from 3–8 to 3–20 are recorded in emission in the CFHT ESPaDOnS spectra; these are also strongly variable, in a manner consistent with the 538-d period.

The basic phenomenology of the variability is, evidently, infilling of a near-normal underlying absorption profile by slightly (∼20–30 km s^{-1}) redshifted, almost symmetrical emission (cf. Fig. 2). This interpretation is consistent both with direct inspection of line profiles, and with the phase dependence of variability; all lines share a common velocity around $\phi_\alpha \simeq 0.5$, becoming increasingly blueshifted with decreasing line strength (i.e., increasing emission infill). Moreover, the amplitude of radial-velocity variation correlates with the amplitude of line-strength variation.

This phenomenology appears to be applicable to almost all variable features, embracing not only the hydrogen and He I lines (including λ6678), but also the signature Of?p C III 4650Å transitions (Fig. 4; the adjacent N III lines are much less, if at all, variable, and so are evidently dominated by 'normal', photospheric, Of emission). He II λ4686 shows an exceptional pattern of variability; narrow emission is present even at quiescent phases, and while the overall emission-line strength increases near phase zero, only small changes occur at the position of this narrow emission (Fig. 4), possibly because the emission is already optically thick here.

4.2 UV P-Cygni profiles

Walborn et al. (2003) presented a high-resolution International Ultraviolet Explorer (IUE) spectrum obtained on 1992 Dec 19 (JD 2,448,975.9, $\phi_\alpha = \overline{9}.74$, $R \simeq 10^4$, $\lambda\lambda \sim$ 1200–1900Å). There are no other high-dispersion UV spectra available, but the IUE archive contains a low-resolution, short-wavelength spectrum (1984 July 25, JD 2,445,907.0, $\phi_\alpha = \overline{14}.04$, $R \simeq 300$). After smoothing and binning the high-resolution spectrum to render it comparable to the low-resolution one (Fig. 5), there is no evidence for *large* changes in the resonance-line profiles of N V λ1240, Si IV λ1400 and C IV λ1550 (although we cannot rule out variations at the moderate level observed in the oblique rotator θ^1 Ori C; Walborn & Nichols 1994). This encourages the view that the Hα variability results from the changing visibility of a constrained plasma, rather than a large-scale global change in outflow characteristics – e.g., if the variability were a consequence of changes in mass-loss rate, this would be expected to have a clear signature in the UV P-Cygni profiles.

5 THE CONSTANT LINES

In contrast to the hydrogen and He I lines, the absorption lines of metals and of He II, together with many selective emission lines, show only small changes, at most, in line strength. For simplicity, we label such lines as 'constant'; if there is any line-strength variability, it is at a very low level.

5.1 Absorption lines

The C IV 5801, 5812Å doublet exemplifies the behaviour of the constant absorption lines. This doublet is particularly well-suited to measurement both on astrophysical grounds (the lines are very symmetrical, and are formed deep in the atmosphere, and hence are less likely to be contaminated by 'windy' emission than many other transitions; cf., e.g., Fullerton et al. 1996), and observationally (the nearby

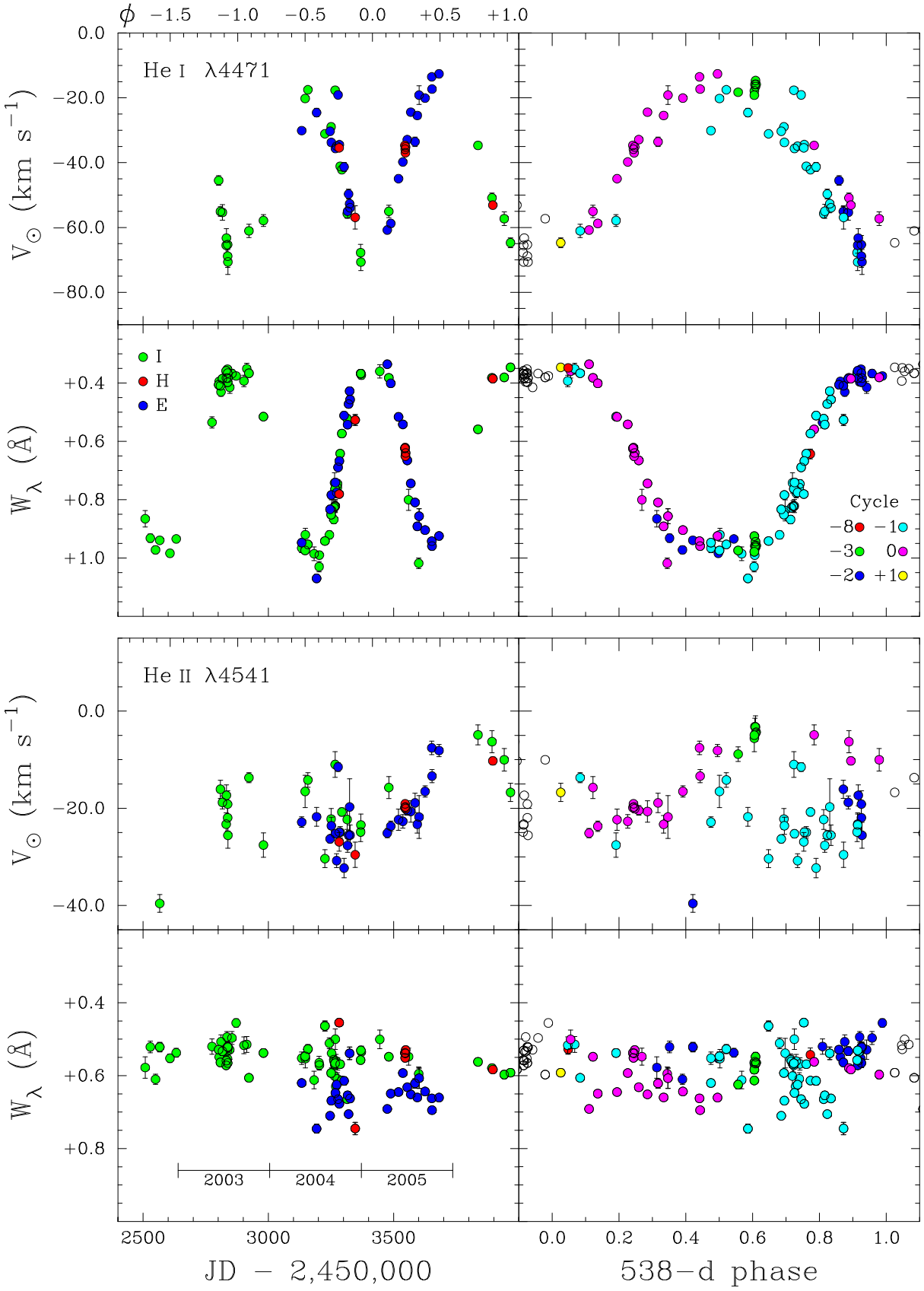

Figure 3. Equivalent-width and velocity variations for He I 4471Å and He II 4541Å. Points with large formal measurement errors are omitted for clarity (so that fewer velocities than line strengths are plotted). As in Fig. 1, the equivalent-width axis is inverted (such that lower points indicate greater absorption/less emission). Points in the left-hand panels are colour coded according to source: E(lodie; Nazé et al. 2007), H(igh-resolution), or I(ntermediate-dispersion). Points in the right-hand panels are colour-coded according to cycle in the ephemeris of eqtn. 2.

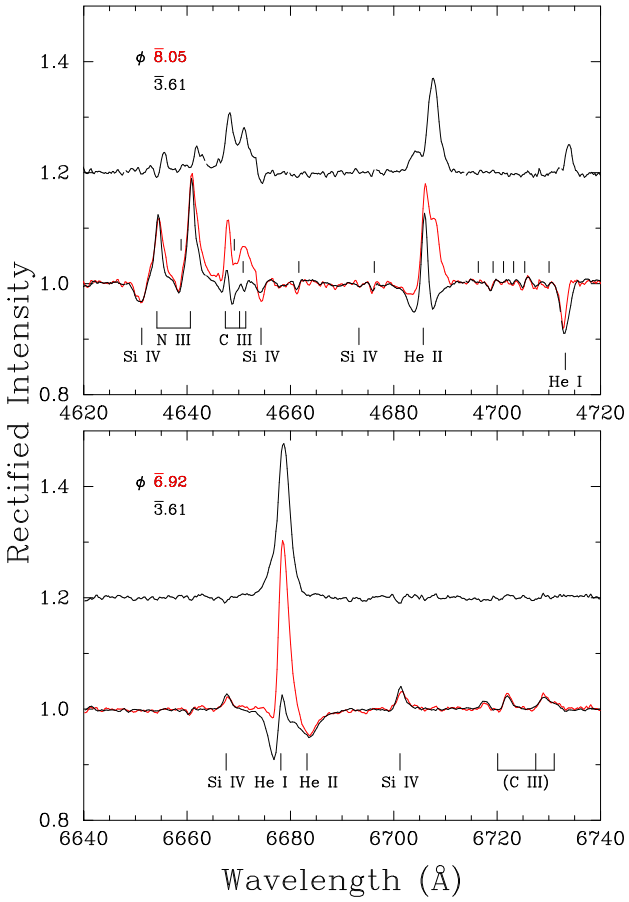

Figure 4. Emission-line variability in HD 191612; spectra are labelled by phase in the Hα ephemeris of eqtn. 2. Data obtained near Hα maximum are shown in red, those near minimum in black; ratio spectra are shown offset by +0.2. (All spectra were obtained near orbital zero; Sec. 5.3.)
Upper panel: the N III 4640Å, C III 4650Å, He II 4686Å emission-line complex; unlabelled tick marks indicate wavelengths of O II lines. Note also the infilling of the red wing of He I 4713Å.
Lower panel: He I/He II 6678/6681Å. Although λ6678 is unusual among the He I lines in showing emission throughout 'quiescence', the qualitative nature of the variability (i.e., growth of a slightly redshifted, fairly narrow emission superimposed on the quiescent-state spectrum) is notable only for the unusually large relative amplitude. The $\lambda\lambda$6717/6722/6729 lines (the latter probably a blend in our data, λ6728.8+6731.1:) are almost constant in strength; the positions appear not to be consistent with a standard C III identification.

diffuse interstellar bands at 5778/5780/5797Å are of similar strength to the C IV lines, and provide a very useful zero-point calibration for the wavelength scale, allowing rather precise differential velocities to be obtained even from intermediate-dispersion data of unexceptional quality).

The C IV measurements are presented in Fig. 6, and illustrate the typical behaviour of essentially constant line strength coupled with small-amplitude radial-velocity variations. The steady increase in velocity between JDs ~2,453,500–700 discussed by Nazé et al. (2007) clearly does not repeat on the 538-d period. Most metal absorption lines strong enough to be measured consistently in most spectra (e.g., N III $\lambda\lambda$4511–4534), as well as the He II absorption

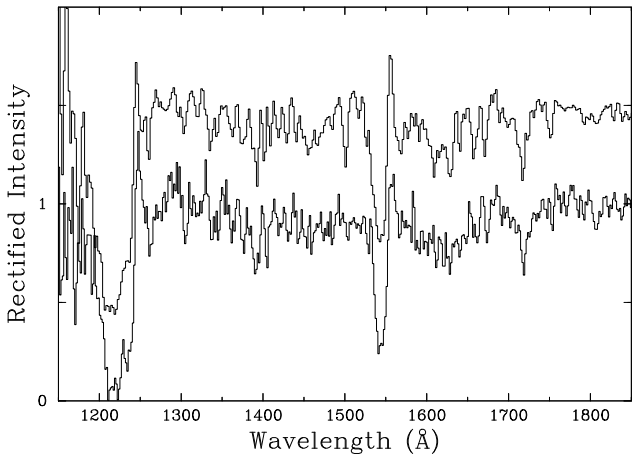

Figure 5. IUE spectra of HD 191612. Lower spectrum, low-resolution, $\phi_\alpha = \overline{14}.04$; upper spectrum (offset by 0.5 continuum units), high-resolution spectrum, $\phi_\alpha = \overline{9}.74$, smoothed and binned to match the low-resolution data.

lines (e.g., $\lambda\lambda$4200, 4541, 5411) follow essentially the same behaviour as the archetypal C IV lines, as illustrated in Fig. 3 by data for He II λ4541.

5.2 Selective emission lines

The high-quality UES and CFHT spectra, in particular, reveal a rich spectrum of selective emission lines (cf. Walborn 2001). In general, the weakness of the lines precludes detailed scrutiny of their phase dependence in the remaining data, but comparison of quiescent and emission-line phases in these echellograms establishes that most of the emission features[7] exhibit essentially the same behaviour as the C IV lines (i.e., near-constant line strength and small-amplitude radial-velocity variations). Only the stronger lines can be consistently measured, but results for Si IV 6667Å shown in in Fig. 6 illustrate the general accord between the behaviours of the selective emissions and the 'constant' absorption lines.

The extensive far-red coverage of the high-quality CFHT ESPaDOnS spectra allows many other weak emission lines to be recognized; these appear also to show little or no variability in line strength (at least, between the two epochs sampled, at 538-d phases 0.24 and 0.89; the 'variable' lines discussed in Section 4 change substantially between these epochs). Most of these features are previously unreported in O-star spectra, and currently lack persuasive identifications. Measured wavelengths in Å (and possible identifications, with multiplet numbers from Moore 1945) are, for the stronger features: 5739.8; 6394.8, 6467.1, 6478.7 (N III 14? good wavelength matches but not all multiplet members present); 6482.3; 7002.8; 7037.2 (C III 6.01); 7306.9; 7455.2; 7515.7; 8019.2 (N III 26); 8103.0 (Si III 37); 8196.6 (C III 43); 8251.0; 8265.7; 8268.9; 8286.8; 9705.5, 9715.4 (both strong, broad; C III 2.01).

[7] Including C II 6578, 6583Å; C III 5696Å; N II 5001/5005, 5667–5680–5686, 6482, 6610Å; N III 5321, 5327Å; Si III(?) 4905.6Å; Si IV 6667, 6701Å; S IV 4486, 4504Å; and the unidentified emission lines first noted by Underhill (1995) at 6717.5, 6722.2, 6729.1 (probably a blend in our data, 6728.8+6731.1:), 6744.4Å.

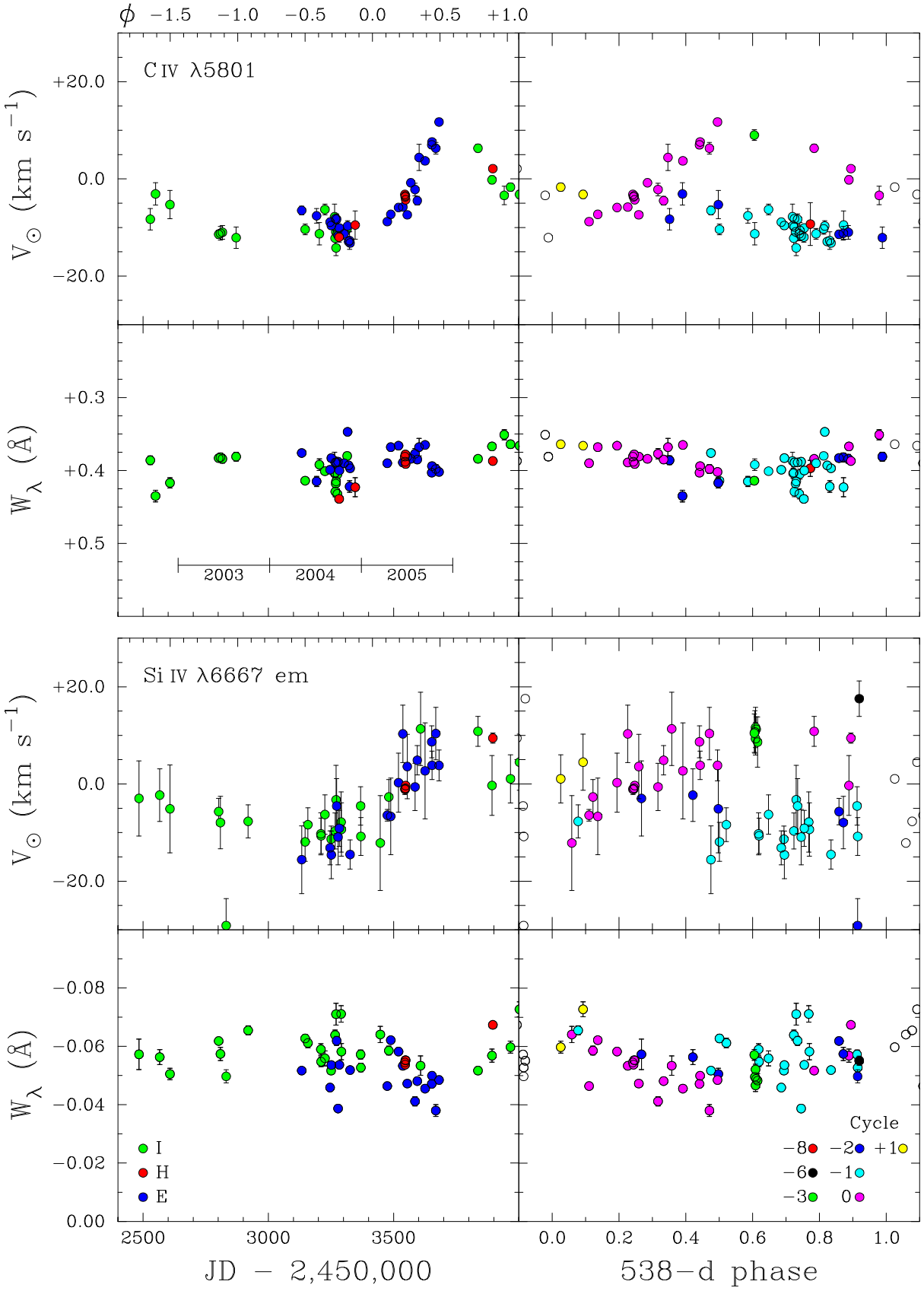

Figure 6. Equivalent-width and velocity variations for the C IV 5801Å absorption and Si IV 6667Å emission lines; other details are as for Fig.3.

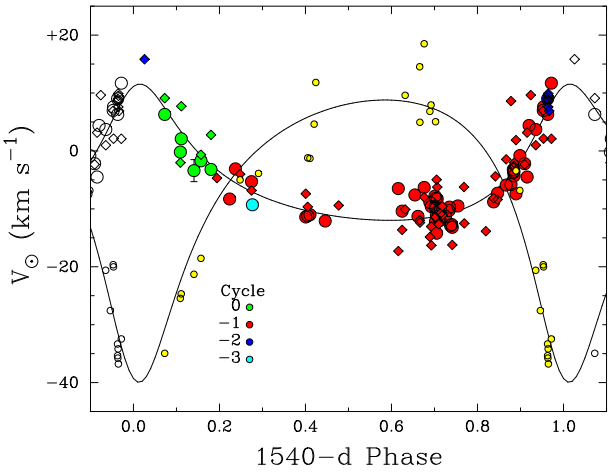

Figure 7. Radial-velocity measurements for C IV 5801Å (large circles), Si IV 6667Å (diamonds), and O II lines (small yellow circles), plotted with the orbital solution of Table 2. The C IV and Si IV points are colour coded according to cycle count in the ephemeris of Table 2, and for display purposes the O II velocities have been adjusted by −14.3 km s^{-1} to bring them to the same γ velocity as the primary (see Sec. 5.3).

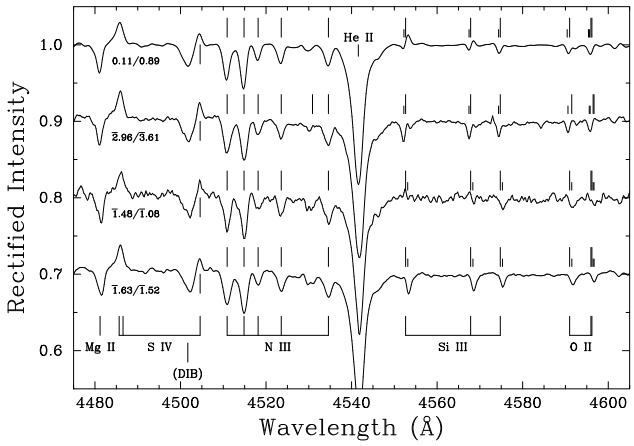

Figure 8. Signatures of the secondary's spectrum. Data have been lightly smoothed, rebinned, and renormalized to facilitate comparison between observations, which are labelled by orbital/Hα phases (Sec. 5.3/3.1). Spectra have been shifted to bring the primary to zero velocity; long tickmarks indicate rest wavelengths of the identified lines. In this reference frame the He II, N III and S IV lines show no significant movement (i.e., arise principally in the primary's spectrum). Short tickmarks show the expected positions of the O II and Si III lines in the secondary spectrum, according to the orbital solution given in Table 2.

5.3 Radial-velocity variations & spectroscopic orbit

The 'constant' lines show significant, systematic radial-velocity variations[8] which do not repeat with the 538-d period (Figs. 3 and 6). These velocity variations cannot reflect photospheric motion about a static centre of mass (the implied change in radius is as great as ∼250R$_\odot$, or ∼17R_*). In principle, they could be attributed to changes in the depth of line formation in the accelerating outflow, through density changes in or near the trans-sonic region resulting from stochastic changes in the stellar-wind mass loss rate. However, the lack of changes in Hα in the mean quiescent spectra around phases $\overline{1}.5$ and 0.5 (corresponding to negative- and positive-velocity C IV states) does not encourage confidence in this interpretation, and we have already argued that the C IV lines are formed relatively deep in the subsonic atmosphere.

We therefore consider the possibility of orbital motion on periods other than that of the major spectroscopic variability. We concentrate on measurements of the C IV 5800Å doublet and the ∼6700Å emission-line complex (Si IV + unidentified), which yield mutually consistent results. Both features have velocity zero-points tied in to nearby, moderately strong diffuse interstellar bands (we adopted DIB wavelengths as measured in the CFHT spectra), and therefore record the velocity variations more precisely and accurately than other lines that lack this advantage. Results are given in Table A2.

Fortuitously, the dataset includes good-quality observations showing that relatively large positive velocities occurred in 538-d cycles −3 and −6, as well as at $\phi_\alpha \sim 0.5$, hinting at $P_{\rm orb} \simeq 3P_\alpha$. Trial orbital solutions with $P_{\rm orb} \simeq$ 1500–1600d yielded residuals that are satisfactorily small, but none the less slightly larger than the formal errors returned by the gaussian fits to lines used to measure velocities. Since external errors evidently dominate (C IV) or match (Si IV) the formal uncertainties, we weighted all C IV measurements and all Si IV measurements equally, but with the Si IV measurements assigned ∼1/3 weight to reflect their greater residuals (and adjusted by −2.1 km s^{-1} to bring them to the same γ velocity as the C IV measurements).

The resulting orbital solution is summarized in Table 2, and illustrated in Fig. 7. While this solution has not yet been subject to the acid test of predictive power, its success in reproducing observations at three separate periastron passages, with small residuals that are consistent with realistic observational uncertainties, encourages the view that the solution does characterize a true binary orbit.

Table 2. Orbital solution. The main orbital parameters are constrained by measurements of C IV 5801Å, Si IV 6667Å in the primary spectrum; K_2 is established from O II lines in the secondary spectrum.

γ	−5.19	±	0.36	km s^{-1}
K_1	11.77		0.84	km s^{-1}
e	0.438		0.038	
ω	344.7		6.5	°
$P_{\rm orb}$	1542		14	d
T_0	JD 2453720		20	
$f(m)$	0.190		0.042	M$_\odot$
$a_1 \sin i$	322		24	R$_\odot$
rms residual	(weight 1, C IV) 2.2 km s^{-1}			
K_2	24.4		1.4	km s^{-1}
$f(m)$	1.68		0.29	M$_\odot$
$a_2 \sin i$	667		38	R$_\odot$
$q = M_2/M_1$	0.483		0.044	
rms residual	(O II) 5.1 km s^{-1}			

[8] The narrow core of He II λ4686 emission, present throughout quiescence, tracks the motion of the 'constant' absorption lines and selective emission lines.

5.3.1 Secondary orbit

Careful examination of weak lines of low ionization stages in the best data shows velocity displacements in antiphase with the stronger lines, bolstering the interpretation of the 1540-d velocity variations as being orbital in origin. The spectroscopic fingerprint of the secondary is weak, but its velocity can be reasonably well quantified by simultaneous gaussian fits to a selection of a half-dozen unblended, relatively strong O II absorption lines ($\lambda\lambda$4300–4700Å, central depths 2–3% below continuum), constrained to share the same velocity shift; results are included in Table A2.

Although we don't have the benefit of well-defined interstellar features to provide a velocity reference for most observations encompassing the O II-line spectral region, we can exploit the fact that the centrally placed He II 4541Å line follows the motion of the C IV and Si IV features used to determine the primary's orbit (Sec. 5.1). By measuring O II velocity *differences* with respect to λ4541, and correcting for computed motion of the primary, we can in effect remove spectrum-to-spectrum velocity zero-point offsets. (Using directly observed velocities gives essentially identical results, but with somewhat larger scatter.)

An orbital solution of the resulting O II velocities gives γ and K_2 (with all other parameters fixed at the primary-orbit values[9]); the slope of He II vs. He II−O II velocities gives an entirely consistent mass ratio. Results are incorporated into Table 2.

5.3.2 Relationship between the 538- and 1540-d periods?

The orbital period is $\sim 3\times538$d, which has suggested to colleagues the possibility of some sort of resonance. However, a solution with $P_{\rm orb} \equiv 3P_\alpha$ gives a significantly poorer fit than one with $P_{\rm orb}$ allowed as a free parameter.[10] Thus although it seems to be quite securely established that HD 191612 is a long-period binary, it appears that, with $P_{\rm orb} = 2.87P_\alpha$, the binary orbit has no important role in the large-amplitude spectroscopic variability.

There is, however, an interplay between the periods in a limited observational sense, explaining otherwise complex behaviour seen in some lines. Fig. 8 shows spectra obtained near the extremes of both the orbital motion and the spectroscopic variability. In addition to illustrating the small orbital velocity amplitudes (less than the line widths) the quiescent-state spectra clearly indicate that absorption in the Si III $\lambda\lambda$4552, 4568, 4575 triplet tracks the secondary spectrum, on the orbital period. The *primary* spectrum has emission in these lines which varies on the 538-d period, and which shows a strong decline in strength going from λ4552 to λ4575 (as is observed in some LBV/WN11 spectra; e.g., He 3-519, Walborn & Fitzpatrick 2000).

The interplay of these two cycles means that the lines can appear purely in absorption (throughout quiescent 538-d phases), but in other states the behaviour is more complex. When the primary and secondary spectra are at or near maximum velocity separation, a P-Cyg-*like* appearance results in $\lambda\lambda$4552, 4568, with absorption in λ4575 (as in the first [top] spectrum in Fig. 8); emission phases at smaller velocity separations can result in apparent disappearance, or nulling, of λ4552 (third spectrum in Fig. 8).

A similar effect is detectable in the N II spectrum, in particular the 5001/5005Å lines, where primary emission and secondary absorption clearly move in antiphase; and, possibly, in the $\lambda\lambda$4414.9, 4417.0 O II lines.

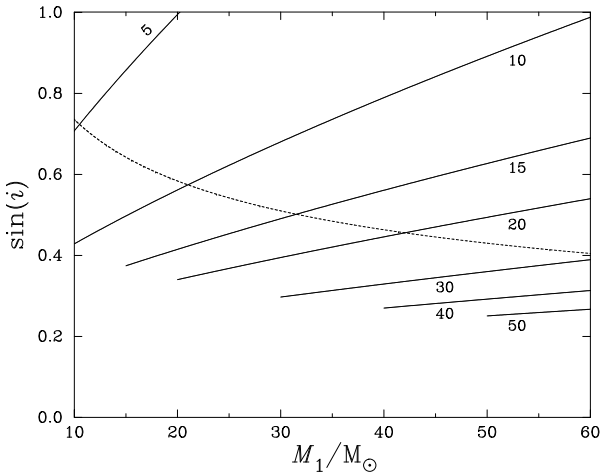

Figure 9. Constraints on the system mass resulting from the orbital solution of Table 2. Solid lines are loci of constant secondary mass, labelled in solar masses, implied by the mass function (assuming $M_2 \leq M_1$); the dotted line shows the estimated mass ratio.

5.4 System characteristics

Mass constraints implied by the orbital solution are illustrated in Fig. 9. We have no constraint on the orbital inclination, but the masses are entirely consistent with a system comprising a ∼30-M$_\odot$, late-O giant accompanied by a ∼15-M$_\odot$, early-B main-sequence star, viewed at an intermediate angle ($\sin i \simeq 0.5$). The projected centres-of-mass separation at periastron is $(1-e)a\sin i = (555\pm68)\mathrm{R}_\odot$ ($\sim 40R_*$); although this certainly allows for the possibility of wind–wind interactions, the Hα emission region, for example, is surely much closer to the primary, so that it is unlikely that the secondary plays any important role in the 538-d changes.

The strong variability of the He I classification lines, together with the small orbital velocity amplitudes (which ensure that the components' helium lines are never resolved in the spectrum) means we cannot estimate the spectral types separately from the spectrum; the *maximum* velocity separation is less than the line widths in the primary. Thus even if the components were as just postulated, with an expected B-band brightness ratio of ∼10:1, the combination of the likely differences in spectral types and the resolution and

[9] For completeness we report that γ velocity for the O II lines is, formally, $+9.1\pm1.0$ km s^{-1}. Although small differences in γ velocities for different lines would not be unusual in an O-type star, it should be noted that our γ velocities for the C IV doublet and the Si IV/λ6700 complex depend on *measured*, (not laboratory) wavelengths for both the reference DIBs and the unidentified λ6700 emissions, while the weakness of the O II lines means that small zero-point shifts arising from, e.g., unrecognised blends would not be surprising.

[10] An F test yields a probability of $\ll$1% that χ^2 for the fixed-period fit is no poorer than that for the solution with $P_{\rm orb}$ free; i.e., formally rules out $P_{\rm orb} \equiv 3P_\alpha$ with $> 99\%$ confidence.

signal:noise of most of our spectra means it is not particularly surprising that we don't see truly double-lined features (other than the peculiar Si III lines noted in section 5.3.2). Nonetheless the O II/Si III lines indicate a secondary spectral type not earlier than B0, and not later than B2 (assuming a dwarf luminosity class and normal composition).

6 OTHER SPECTROSCOPIC PROPERTIES

6.1 Spectral classification

Our extended dataset, and improved understanding of the spectroscopic variability, allow us to revisit the spectral classification (that is, the classification of the *spectrum* – not the component stars).

The $\phi_\alpha = 0$ spectrum (specifically, the WHT spectrum of JD 2453941.5) yields spectral type O6.5f?pe ('O6.5' from the He I 4471/He II 4541 ratio, with qualifiers 'f?p' from C III λ4650 and 'e' from the Hγ emission). Our refined classification of the quiescent-state spectra is O8fp (the weakness of C III in that state excluding Of?p). Of course, it is now clear that these apparent variability in spectral type does not reflect changes in any fundamental stellar properties – which would result in large-amplitude photometric variability – but instead results from infilling of the He I λ4471 classification line by emission.

These results are in full accord with previous classifications, including in particular Walborn's original blue-region spectrum, obtained on 1972 Sept. 24 ($\phi_\alpha = \overline{22}.02$) and also classified O6.5f?pe (Walborn 1973) – consistent with the underlying 'clock' keeping good time for at least a decade before the earliest digital data.

Luminosity classification at any state is not possible because of the unique, peculiar profile of the fundamental He II 4686Å criterion. The strength of Si IV 4089Å relative to nearby He I lines would be consistent with luminosity class V, while the UV Si IV resonance doublet is neither dwarf- nor supergiant-like, but is possibly consistent with class III. The physical properties established in Section 6.3 are also broadly giant-like. However, all the known Of?p stars are sufficiently spectroscopically peculiar that any luminosity-class argument based on direct comparisons with normal stars must be considered hazardous.

6.2 Spectroscopic fine analysis

Although the peculiarities of the spectra preclude extremely detailed modelling, the basic photospheric parameters can none the less be quite well constrained. We searched for matches to the 'quiescent' spectrum of 2001 Aug 5 ($\phi_\alpha = \overline{3}.61$), using a grid of FASTWIND models (Puls et al. 2005) sampled at steps of 1kK and 0.2 in $T_{\rm eff}$ and $\log g$ (with $Y = 0.1$ and $v_{\rm turb} = 15$ km s^{-1}). We find a generally good match with observations for a model with $T_{\rm eff} = 35.0$kK, $\log g = 3.5$, in excellent agreement with the analysis reported by Walborn et al. (2003, conducted by AH but based on simpler models and poorer-quality data).

No model reproduces the strength of He I 4471Å (cf. the general discussion of this issue by Repolust et al. 2004), but the He I singlet lines are fully consistent with the estimated $T_{\rm eff}$; adopting 34kK would still require $\log g = 3.5$, but leads to the model He II lines becoming too weak. The best-fit model parameters can therefore be considered as fairly well determined, to $\sim \pm$1kK, 0.1 in $T_{\rm eff}$, $\log g$ (although, of course, no model matches the peculiar He II 4686, He I 6678Å profiles).

This takes no account of the effect of the secondary spectrum, which is expected to have somewhat stronger He I lines, while the He II line strengths may be underestimated by ∼10% through dilution. This would result in the primary being, if anything, modestly warmer (by perhaps ∼1kK) than the foregoing analysis suggests.

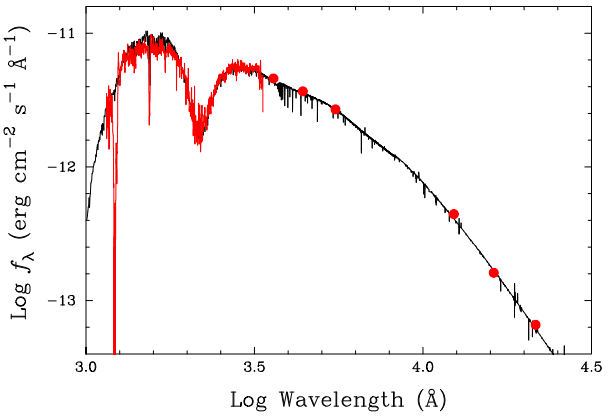

Figure 10. Spectral-energy distribution for HD 191612 (red). The weighted sum of an OSTAR2002 model with $T_{\rm eff} = 35$kK, $\log g = 3.5$ and an ATLAS9 model with $T_{\rm eff} = 20$kK, $\log g = 4.5$, with a V-band flux ratio of 9:1 and $E(B-V) = 0.56$, is shown for comparison (black; see Section 6.3 for details).

6.3 Reddening, radius

To determine the reddening and angular diameter we compared a $T_{\rm eff} = 35.0$kK, $\log g = 3.5$ OSTAR2002 model (Lanz & Hubeny 2003) with archival low-resolution IUE spectrophotometry and optical & 2MASS photometry. We estimate $(R_{\rm eff}/{\rm R}_\odot)/(D/{\rm kpc}) = 6.7 \pm 0.05$ and $E(B-V) = 0.56 \pm 0.03$ [using a Cardelli et al. 1989 reddening law with $R_V \equiv A(V)/E(B-V) = 3.1$]; here $R_{\rm eff}$ is an 'effective' radius characterizing the emitting surfaces. The match between the model and observations, though not perfect, is reasonably good, and there is no evidence of any IR excess out to 2μm. The fit is slightly improved by allowing for the contribution of a cooler secondary, such as a ∼20kK secondary contributing ∼10% of the light at V, and this *ad hoc* model is illustrated in Fig. 10.

The reddening and general properties are consistent with membership of the Cyg OB3 association, as noted by Humphreys (1978); we adopt her association distance of 2.29 kpc (see discussion in Walborn 2002 for the embedded cluster NGC 6871), whence the primary's radius is

$$R_* \simeq 14.5 \sqrt{\frac{f_1}{0.9}} \left(\frac{d}{2.3\,{\rm kpc}}\right) \left(\frac{35{\rm kK}}{T_{\rm eff}}\right) 10^{+0.2\left[\frac{R_V}{3.1}\,\frac{E(B-V)}{0.56}\right]} {\rm R}_\odot,$$

where f_1 is the fractional V-band luminosity of the primary and the $T_{\rm eff}$ term accounts for the approximate $T_{\rm eff}^2$ scaling of model-atmosphere V-band surface fluxes in this temperature range. The primary then has $\log(L/{\rm L}_\odot) \simeq 5.4$ and

$M(V) \simeq -5.6$ – parameters broadly consistent with a late-O giant.

6.4 Hα mass-loss rate

In our FASTWIND models the mass-loss rate is characterized by a parameter

$$Q = \frac{\dot{M}\sqrt{f_{\rm cl}}}{\mathrm{M_\odot yr^{-1}}} \Bigg/ \left(\frac{v_\infty}{\mathrm{km\ s^{-1}}}\frac{R_*}{\mathrm{R_\odot}}\right)^{1.5}$$

(Puls et al. 2005), where $f_{\rm cl} = \langle\rho^2\rangle / \langle\rho\rangle^2$ is the clumping factor; from modelling of Hα, we find $-\log Q = 12.6$–12.7 for the minimum-state spectrum. We estimate $v_\infty \simeq 2700$ km s^{-1} (with $\sim$10–15% uncertainty) from the C IV resonance doublet in the IUE spectra, whence the primary's quiescent stellar-wind mass loss rate is $\log\left(\dot{M}\sqrt{f_{\rm cl}}\right) \simeq -5.8$ dex M$_\odot$yr^{-1}. As for other aspects of the FASTWIND analysis, this is in satisfactory agreement with the corresponding result reported by Walborn et al. (2003; $\dot{M} = -5.6$ dex M$_\odot$yr^{-1}).

6.5 Rotation

The equatorial velocity expected for a 538-d rotation period and $R_* \simeq 14.5$R$_\odot$ is $\sim$1.4 km s^{-1}, and a measurement of $v_{\rm e}\sin i$ would provide a strong test of rotational modulation. (For reference, the equatorial rotation velocity for synchronous rotation is $\sim$0.5 km s^{-1}, or, for pseudosynchronous [periastron-synchronized] rotation, $\sim$0.8 km s^{-1}.) Most lines in the spectrum show asymmetries or variability to some extent, but, as already discussed, the C IV 5800Å doublet shows exceptionally symmetrical profiles with little or no evidence of contamination by emission; these high-excitation lines are expected to form rather deep in the atmosphere, and therefore to be more representative of the subsonic photosphere than many other features.

Donati et al. (2006a; see also Howarth 2003) showed that the C IV profiles deviate strongly from those expected from rotational broadening, but are well matched by simple gaussian 'turbulence', with zero rotation. We have attempted to set upper limits to the rotation rate by looking for zero-amplitude nodes in the fourier transform of the profiles (Gray 1992) in the combined 2005 CFHT spectra (s:n $> 10^3$). We compared the results with transforms of synthetic spectra that include rotational broadening, isotropic gaussian macroturbulence, and gaussian noise, using an intrinsic profile from an OSTAR2002 model (Lanz & Hubeny 2003).

Illustrative results are shown in Fig. 11. Even for these very high-quality results there is no sign of rotational zeroes above the noise (which dominates at frequencies $\gtrsim 10^{-2}$ s km^{-1}). Empirically, we find that the observations are well matched by any model having

$$\sqrt{\sigma_{\rm V}^2 + (v_{\rm e}\sin i/2)^2} \simeq 45\ \mathrm{km\ s^{-1}}$$

(where $\sigma_{\rm V}$ characterizes the velocity dispersion of the macroturbulence and $v_{\rm e}\sin i$ characterizes the projected equatorial rotation velocity), for $v_{\rm e}\sin i \lesssim 60$ km s^{-1}; larger values of $v_{\rm e}\sin i$ are ruled out by the data. This is a disappointingly weak upper limit given the data quality, but results from the effectiveness of the gaussian turbulence in removing information with high spatial frequencies from the profiles.

7 DISCUSSION

The symmetry and reproducibility of, in particular, the Hα 538-d light-curve strongly suggest an origin in an essentially geometrical process – i.e., the changing aspect of a distinct emission region. This is also consistent with the absence of evidence of associated global changes in stellar-wind properties (Sec. 4.2). Since we have found that the variability is not orbital, our results lend strong support to the proposal by Donati et al. (2006a) of rotationally modulated line emission from a magnetically constrained plasma.

One might hope that the fairly rich emission spectrum would offer insight as to conditions in the line-forming region, but there is a dearth of traditional nebular diagnostics (suggesting a high-density regime). We can only infer some general characteristics of the Hα-emitting region. First, optically thin Hα emission in an *any* time-independent axisymmetric structure cannot account for the observed 538-d behaviour; at least half the emission from any such structure would visible at all times, but emission equivalent to the adopted 'excess' emission cannot plausibly be present during 'quiescent' phases. At the same time, very complex geometries (such as observed in τ Sco; Donati et al. 2006b) are unlikely, as they would not be consistent with the large amplitude of emission variability.

Secondly, for the distance and reddening adopted in Section 6.3, and assuming isotropic, case-B recombination emission, the maximum excess Hα emission over the quiescent state corresponds to

$$\int n_{\rm e}^2\,\mathrm{d}V \simeq 7\times10^{22}\mathrm{cm^{-6}}R_*^3.$$

This is a lower limit to the true emission measure if the emission is not optically thin.

If we adopt the hypothesis that the geometry of the line-emitting region is determined by the magnetic field, then the simplest acceptable magnetic-field geometry is a misaligned, centred dipole – known to provide a reasonable approximation to θ^1 Ori C, the prototype magnetic O star (Stahl et al. 1996; Donati et al. 2002; Wade et al. 2006). Babel & Montmerle (1997) argue that, for such a geometry, stellar-wind material from the magnetic polar and temperate regions will be deflected along the field lines towards the magnetic equator, where the colliding flows shock to create a high-temperature, X-ray emitting plasma. The plasma cools to form a dense disc which gives rise to optical emission. MHD calculations support this general outline, albeit with a number of refinements (e.g., ud-Doula & Owocki 2002; Gagné et al. 2005; ud-Doula et al. 2006).

Since this model is at least consistent with the direct magnetic-field measurements of HD 191612 (Donati et al. 2006a), for heuristic purposes we explore schematic 'toy' models of Hα emission from a centred, tilted, geometrically thin disk, in which the relative emission is simply related to the projected area (taking into account limb darkening and occultation by the star). Although this is a physics-free, geometrical model, we can speculate that it may characterize a more realistic scenario; e.g., for a disk-like emission region,

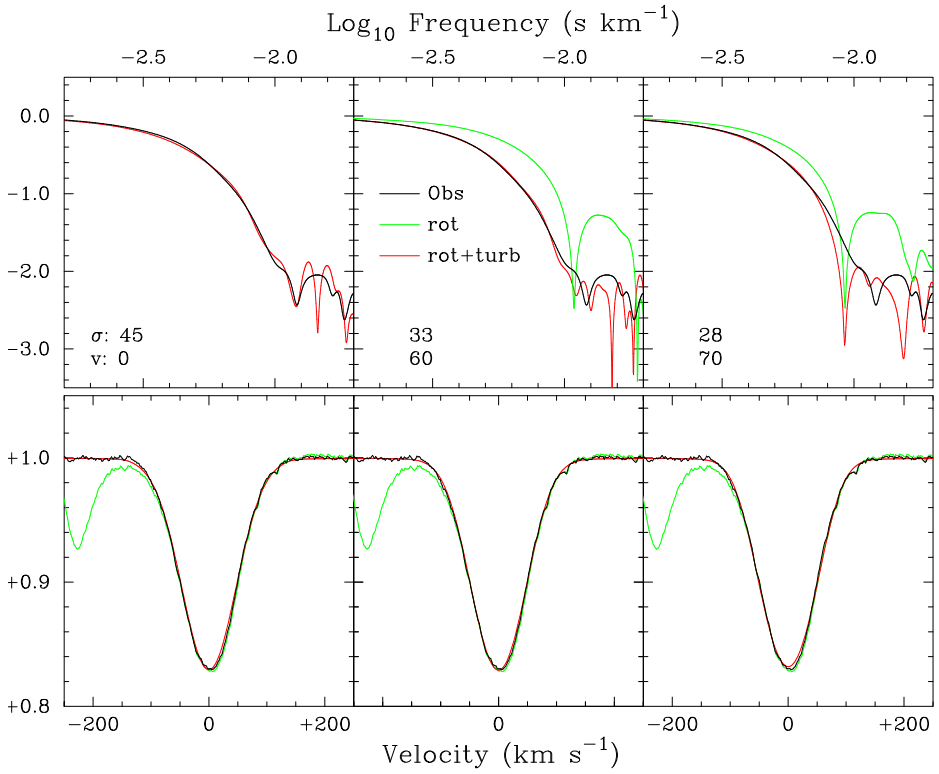

Figure 11. Illustrative line-broadening models for the C IV 5801Å line.
Upper panels: results in the fourier domain. Solid black lines show the transform of the observed profile (i.e., the transform of the black spectrum in the lower panels); red lines show the transforms of synthetic profiles computed with isotropic gaussian macroturbulence (with dispersion σ, in km s^{-1}), rotational broadening (with $v_{\rm e} \sin i$ = v), and gaussian noise; and green lines show the transforms for rotational broadening alone. Any model with $v_{\rm e} \sin i \lesssim 60$ km s^{-1} (and appropriate macroturbulence) is acceptable.
Lower panels: results in the wavelength domain. The observed spectrum is shown in each panel in green (the directly observed profile) and black (the version of the profile used in the analysis, after re-rectification to take out the diffuse interstellar band). The synthetic profiles, shown in red, are the inverse transforms of the models shown in red in the upper panels. At this scale, the synthetic profiles (which have been modestly scaled in intensity to match the observed line strength) are almost indistinguishable from each other, and from the observed spectrum, in the wavelength domain.

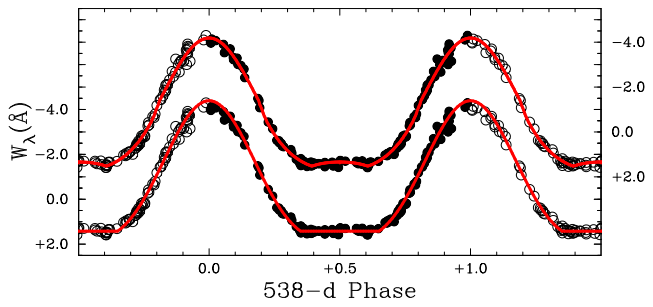

Figure 12. 'Toy' models compared to phased Hα equivalent widths (circles). Lower model (left-hand axis), a single surface 'spot'; upper model (right-hand axis), an optically thick disk. See section 7 for details.

the 'limb darkening' may actually correspond to increasing Hα optical depth as the line of sight approaches the plane of the disk.

We find that this simple model can provide a reasonable match to the Hα variability, provided that (i) the sum of the inclination of the rotational axis to the line of sight and the angle between that axis and the magnetic axis is close to 90°, and (ii) moderately strong limb-darkening is present (so that the emission is low at all rotational phases when the line of sight is close to the disk plane). Moreover, the width:thickness ratio must be reasonably large, to account for the large amplitude of emission-line variability.

A specific model, selected through a genetic-algorithm minimization, is shown in Fig. 12; its parameters are inner radius $R_{\rm in} = 2.00 R_*$, outer radius $R_{\rm out} = 2.13 R_*$, axial inclination $i = 68°$, magnetic-axis offset $\alpha = 27°$, and linear limb-darkening coefficient $u = 0.7$. These parameters should be regarded only as illustrative, as many other combinations give closely similar fits (e.g., $1.55 R_*$, $1.76 R_*$, 41°, 56°, 0.6 gives results almost indistinguishable from those in Fig. 12). The radii, in particular, are only very weakly constrained from the Hα light-curve, because the total emission is fixed by an arbitrary scaling factor (parametrizing the surface emissivity).

[In principle, the continuum photometry could help fix the radii, but in practice it only weakly constrains the model, because the photometric amplitude is so small, the noise is relatively high, and the number of free parameters is large. The only firm conclusion is that a very large disk, very close

to the star, and optically thick in the continuum, is not allowed. The broad-band photometry suggests that any disk cannot contribute more than ∼3–4% of the visible-region broad-band (H_P) flux – that is, the implied equivalent width of the Hα emission referred to disk continuum is as much as ∼150Å.]

The toy model succeeds in reproducing the Hα light-curve, but it would clearly be rash to put too much weight on this success. Not only does the physical model which inspired it encounter difficulties in accounting for the details of the observed X-ray emission (Nazé et al. 2007), but also the disk model is certainly not unique. To illustrate this, we have also considered a minimalist model of Hα emission from a single surface spot,[11] described by

$$f_\alpha = f_0 + A(\cos i \cos\beta + \sin i \sin\beta \cos\phi)(1 - u + u\cos\mu),$$

where f_0, A are normalizing constants, i is the inclination of the rotation axis to the line of sight, β is the colatitude of the spot, ϕ is the rotational phase, u is a linear limb-darkening coefficient, and μ is the angle between the line of sight and the surface normal at the spot. We find that the form of the Hα light-curve can again be well matched by this model, with $u \simeq 0.6$, $i + \beta \simeq 105°$, $i \simeq \beta$ (Fig. 12).

8 SUMMARY AND CONCLUSIONS

We have shown that the O6.5f?pe–O8fp spectroscopic variations observed in HD 191612 are underpinned by an extremely regular 538-d 'clock' which has kept good time across 24 years of quantitative data (and which is documented a decade further back by photographic material). The Balmer and He I lines show changes which are highly reproducible on this period, and which are characterized by variations in slightly redshifted, moderately narrow 'excess' emission. Absorption lines of metals and He II are essentially constant in line strength (as are many selective emission lines), but show radial-velocity changes arising in a double-lined spectroscopic-binary orbit with $P_{\rm orb} = 1542$d. The components' properties are broadly in accord with an ∼O8 giant-like primary and a ∼B1 main-sequence companion.

The results are entirely consistent with the 538-d variability arising through rotational modulation of a magnetically-constrained plasma, as proposed by Donati et al. (2006a). As in the case of the B0.2 V star τ Sco (Donati et al. 2006b), the implied slow rotation and the long-term stability of the variations argue that the field originates in a fossil remnant, rather than a dynamo. However, although toy 'disk' models (among others) are consistent with some aspects of the data, we are unable to constrain the geometry of the emission region in an interesting way. Future work could therefore usefully concentrate on improving our understanding of the field geometry, which should provide a better framework for numerical models of optical emission, and perhaps help resolve the issues of anomalously broad X-ray lines and soft X-ray emission reported by Nazé et al. (2007). A continuing programme of circular spectropolarimetry is working towards this aim, and a magnetic-field measurement from the second-epoch ESPaDOnS observation used here already gives a clearly detected field with a longitudinal component larger than the discovery measurement, as expected for the geometry adopted by Donati et al. (2006a) and in our toy disk model.

[11] Though it lacks any compelling physical underpinning, this 'spot' model was partly motivated by analogy with magnetic oblique rotators; of course, a centred oblique dipole would be expected to give rise to *two* 'spots', one of which would be visible at any phase.

ACKNOWLEDGEMENTS

We thank all the observers who contributed spectra to this campaign; the service observers at the Isaac Newton Group; Sergio Ilovaisky and Ashok K. Pati for orchestrating spectroscopy at OHP and VBO; Roger Griffin for comments on the orbital solutions; and our referee, Otmar Stahl, and his colleagues at the Landessternwarte Heidelberg for establishing the date of Peppel's observation from the original logs. We also gratefully acknowledge the following for support: the FNRS, PRODEX/Belspo, and OPTICON (YN, GR); the Estonian Science Foundation, Grant 6810 (KA, IK); and the F.H. Levinson fund of the Peninsula Community Foundation (DM).

REFERENCES

Babel J., Montmerle T., 1997, ApJL, 485, L29
Cardelli J. A., Clayton G. C., Mathis J. S., 1989, ApJ, 345, 245
Donati J.-F., Babel J., Harries T. J., Howarth I. D., Petit P., Semel M., 2002, MNRAS, 333, 55
Donati J.-F., Howarth I. D., Bouret J.-C., Petit P., Catala C., Landstreet J., 2006, MNRAS, 365, L6
Donati J.-F., Howarth I. D., Jardine M. M., Petit P., Catala C., Landstreet J. D., Bouret J.-C., Alecian E., Barnes J. R., Forveille T., Paletou F., Manset N., 2006, MNRAS, 370, 629
Evans C. J., Howarth I. D., Irwin M. J., Burnley A. W., Harries T. J., 2004, MNRAS, 353, 601
Fullerton A. W., Gies D. R., Bolton C. T., 1996, ApJS, 103, 475
Gagné M., Oksala M. E., Cohen D. H., Tonnesen S. K., ud-Doula A., Owocki S. P., Townsend R. H. D., MacFarlane J. J., 2005, ApJ, 628, 986
Gray D. F., 1992, The observation and analysis of stellar photospheres. Cambridge University Press
Howarth I. D., 2003, in Maeder A., Eenens P., eds, ASP Conf. Ser. 215: IAU Symp: Stellar Rotation p. 33
Humphreys R. M., 1978, ApJS, 38, 309
Kaper L., Henrichs H. F., Fullerton A. W., Ando H., Bjorkman K. S., Gies D. R., Hirata R., Kambe E., McDavid D., Nichols J. S., 1997, A&A, 327, 281
Koen C., Eyer L., 2002, MNRAS, 331, 45
Lanz T., Hubeny I., 2003, ApJS, 146, 417
Massey P., Duffy A. S., 2001, ApJ, 550, 713
Moore C. E., 1945, A Multiplet Table of Astrophysical Interest, Princeton University Observatory, 20, D1
Morel T., Marchenko S. V., Pati A. K., Kuppuswamy K., Carini M. T., Wood E., Zimmerman R., 2004, MNRAS, 351, 552
Nazé Y., 2004, PhD thesis, Université de Liège

Nazé Y., Rauw G., Pollock A. M. T., Walborn N. R., Howarth I. D., 2007, MNRAS, 375, 145
Peppel U., 1984, A&AS, 57, 107
Puls J., Urbaneja M. A., Venero R., Repolust T., Springmann U., Jokuthy A., Mokiem M. R., 2005, A&A, 435, 669
Repolust T., Puls J., Herrero A., 2004, A&A, 415, 349
Stahl O., Kaufer A., Rivinius T., Szeifert T., Wolf B., Gaeng T., Gummersbach C. A., Jankovics I., Kovacs J., Mandel H., Pakull M. W., Peitz J., 1996, A&A, 312, 539
ud-Doula A., Owocki S. P., 2002, ApJ, 576, 413
ud-Doula A., Townsend R. H. D., Owocki S. P., 2006, ApJL, 640, L191
Underhill A. B., 1995, ApJS, 100, 433
Wade G. A., Fullerton A. W., Donati J.-F., Landstreet J. D., Petit P., Strasser S., 2006, A&A, 451, 195
Walborn N., 2001, in Gull T. R., Johannson S., Davidson K., eds, ASP Conf. Ser. 242: Eta Carinae and Other Mysterious Stars: The Hidden Opportunities of Emission Spectroscopy p. 217
Walborn N. R., 1973, AJ, 78, 1067
Walborn N. R., 2002, AJ, 124, 507
Walborn N. R., Fitzpatrick E. L., 2000, PASP, 112, 50
Walborn N. R., Howarth I. D., Herrero A., Lennon D. J., 2003, ApJ, 588, 1025
Walborn N. R., Howarth I. D., Rauw G., Lennon D. J., Bond H. E., Negueruela I., Nazé Y., Corcoran M. F., Herrero A., Pellerin A., 2004, ApJL, 617, L61
Walborn N. R., Lennon D. J., Heap S. R., Lindler D. J., Smith L. J., Evans C. J., Parker J. W., 2000, PASP, 112, 1243
Walborn N. R., Nichols J. S., 1994, ApJL, 425, L29

APPENDIX A: OBSERVATIONAL DETAILS

This appendix summarizes

- The log of observations (Table A1, available in full online)
- Radial-velocity measurements used in the orbital solutions (Table A2)

Table A1. Format of Table A1 (available in full on-line), the log of optical spectroscopy used in this paper. Each 'observation' is a dataset collected at a single site in a given night, and may consist of several separate spectra. Phases are calculated with the ephemerides of Table 2 and eqtn. 2; the notation $\overline{C}.ppp$ means phase $+.ppp$ in cycle $-C$. Where two observers are identified, the second name is the PI or instigator of the observation; 'srv' indicates a service-mode observation. Where observers provided smoothed or binned spectra, the effective resolution is tabulated ($\Delta\lambda$).

JD	Year	Phase ϕ_α (Hα)	Phase φ (orb)	λ range (nm)	Telescope/ Instrument	Observer	$\Delta\lambda$ (Å)	W_λ(Hα) (Å)
2447691.5	1989.45	$\overline{11}.35$	$\overline{4}.09$	651–662	INT/IDS	Prinja/Howarth	0.5	+1.37
2447724.7	1989.54	$\overline{11}.42$	$\overline{4}.11$	404–499	INT/IDS	Herrero	0.8	
2447726.5	1989.55	$\overline{11}.42$	$\overline{4}.11$	634–677	INT/IDS	Herrero	1.5	+1.41
2448117.4	1990.62	$\overline{10}.15$	$\overline{4}.37$	394–474	INT/IDS	Howarth	1.5	
2449139.7	1993.41	$\overline{8}.05$	$\overline{3}.03$	439–481	INT/IDS	Vilchez	0.5	
⋮	⋮	⋮	⋮	⋮	⋮	⋮	⋮	⋮
2453955.4	2006.60	1.00	0.15	637–673	Tartu	Kolka	1.5	−4.00
2453956.5	2006.60	1.01	0.15	637–673	Tartu	Kolka	1.5	−3.96
2453958.4	2006.61	1.01	0.15	637–673	Tartu	Kolka	1.5	−4.14
2453966.6	2006.63	1.03	0.16	384–706	WHT/ISIS	Leisy/Lennon	0.4	−4.07
2454002.5	2006.73	1.09	0.18	384–706	WHT/ISIS	Leisy/Lennon	0.4	−3.32

Table A2. Velocities used in orbital solutions. Note that each of the three datasets is subject to a separate velocity zero-point error of order a few km s^{-1} (see footnote 9).

JD	$V_\odot$ km s^{-1}	JD	$V_\odot$ km s^{-1}	JD	$V_\odot$ km s^{-1}	JD	$V_\odot$ km s^{-1}	JD	$V_\odot$ km s^{-1}
C IV 5800Å									
2449529.4	−9.3	2453203.5	−11.3	2453275.2	−11.3	2453474.6	−8.8	2453601.4	+4.4
2452127.5	+9.0	2453225.8	−6.3	2453276.2	−10.6	2453488.6	−7.3	2453625.4	+3.7
2452528.8	−8.3	2453246.3	−8.9	2453278.3	−11.7	2453519.6	−5.9	2453652.3	+7.0
2452549.4	−3.1	2453251.3	−9.6	2453282.4	−12.0	2453536.7	−5.8	2453653.3	+7.6
2452607.3	−5.3	2453264.3	−7.8	2453283.3	−10.1	2453545.0	−3.2	2453668.3	+6.3
2452801.6	−11.4	2453265.3	−9.6	2453302.3	−11.3	2453546.0	−3.7	2453681.3	+11.7
2452808.5	−11.2	2453266.3	−12.2	2453314.6	−10.3	2453547.0	−3.5	2453836.8	+6.3
2452816.6	−11.0	2453267.2	−9.9	2453316.3	−9.7	2453548.0	−4.3	2453892.7	−0.2
2452871.2	−12.1	2453267.4	−8.2	2453320.3	−12.9	2453554.6	−7.4	2453896.0	+2.1
2453132.9	−6.5	2453269.2	−10.9	2453324.3	−12.7	2453568.5	−0.8	2453941.5	−3.4
2453146.7	−10.4	2453270.2	−14.2	2453326.3	−13.2	2453585.5	−2.2	2453966.6	−1.7
2453192.5	−7.6	2453272.4	−8.3	2453346.4	−9.5	2453594.5	−4.5	2454002.5	−3.2
λ6700 emission									
2450683.5	−9.4	2452808.5	−34.8	2453266.6	−36.6	2453474.6	−33.3	2453594.5	−22.0
2452127.4	−16.4	2452919.3	−34.6	2453270.2	−30.2	2453480.7	−29.6	2453607.4	−15.6
2452128.4	−16.2	2453132.9	−42.5	2453272.4	−31.4	2453488.6	−33.6	2453625.4	−24.2
2452129.4	−17.6	2453146.7	−38.8	2453278.3	−37.8	2453519.6	−26.6	2453652.3	−18.2
2452129.6	−15.3	2453157.7	−35.3	2453283.3	−36.0	2453536.7	−16.6	2453653.3	−23.1
2452130.4	−15.6	2453209.7	−37.2	2453290.6	−34.7	2453545.0	−28.0	2453668.3	−16.5
2452132.7	−18.3	2453210.5	−37.6	2453291.6	−36.2	2453546.0	−28.0	2453681.3	−23.1
2452483.6	−29.9	2453225.8	−33.2	2453326.3	−41.4	2453547.0	−27.8	2453836.8	−16.1
2452566.3	−29.2	2453246.3	−40.0	2453368.3	−31.4	2453548.0	−27.2	2453892.7	−27.2
2452607.3	−32.0	2453250.5	−38.2	2453369.3	−37.7	2453554.6	−23.3	2453896.0	−17.5
2452801.6	−32.6	2453251.3	−41.5	2453446.7	−39.0	2453585.5	−27.5	2453966.6	−25.8
O II absorption									
2452101.6	−28.7	2452566.3	−24.6	2453157.7	+21.6	2453266.6	+19.7	2453681.3	−35.1
2452127.4	−33.0	2452632.3	−5.9	2453209.7	+15.7	2453554.6	−6.6	2453836.8	−32.7
2452127.5	−33.5	2452808.5	+7.2	2453210.5	+6.9	2453568.5	−11.1	2453892.7	−21.4
2452128.4	−33.4	2452816.6	+5.7	2453225.8	+11.3	2453625.4	−26.3	2453896.0	−23.4
2452129.4	−32.7	2452831.6	+6.1	2453246.3	+5.0	2453652.3	−19.1	2453941.5	−17.2
2452130.4	−34.9	2452837.6	+14.3	2453250.5	+11.6	2453653.3	−25.8	2453966.6	−20.4

Table A1. Optical spectroscopy used in this paper. Each 'observation' is a dataset collected at a single site in a given night, and may consist of several separate spectra. Phases are calculated with the ephemerides of Table 2 and eqtn. 2; the notation $\overline{C}.ppp$ means phase $+.ppp$ in cycle $-C$. Where two observers are identified, the second name is the PI or instigator of the observation; 'srv' indicates a service-mode observation. Where observers provided smoothed or binned spectra, the effective resolution is tabulated ($\Delta\lambda$).

JD	Year	Phase ϕ_α (Hα)	Phase φ (orb)	λ range (nm)	Telescope/ Instrument	Observer	$\Delta\lambda$ (Å)	W_λ(Hα) (Å)
2447691.5	1989.45	$\overline{11}$.35	$\overline{4}$.09	651–662	INT/IDS	Prinja/Howarth	0.5	+1.37
2447724.7	1989.54	$\overline{11}$.42	$\overline{4}$.11	404–499	INT/IDS	Herrero	0.8	
2447726.5	1989.55	$\overline{11}$.42	$\overline{4}$.11	634–677	INT/IDS	Herrero	1.5	+1.41
2448117.4	1990.62	$\overline{10}$.15	$\overline{4}$.37	394–474	INT/IDS	Howarth	1.5	
2449139.7	1993.41	$\overline{8}$.05	$\overline{3}$.03	439–481	INT/IDS	Vilchez	0.5	
2449529.4	1994.48	$\overline{8}$.77	$\overline{3}$.28	445–603	WHT/ISIS	Crowther	1.5	
2450683.5	1997.64	$\overline{6}$.92	$\overline{2}$.03	356–407 641–677	WHT/UES	Trapero	0.07, 0.13	−3.82
2452101.6	2001.52	$\overline{3}$.56	$\overline{2}$.95	369–535	INT/IDS	Erwin/Herrero	0.20	
2452127.4	2001.59	$\overline{3}$.60	$\overline{2}$.97	388–482 636–676	WHT/ISIS	Evans/Howarth	0.5, 0.8	+1.58
2452127.5	2001.59	$\overline{3}$.60	$\overline{2}$.97	361–599	WHT/UES	Evans/Howarth	0.06	
2452128.4	2001.60	$\overline{3}$.61	$\overline{2}$.97	388–477 636–676	WHT/ISIS	Evans/Howarth	0.5, 0.8	+1.59
2452129.4	2001.60	$\overline{3}$.61	$\overline{2}$.97	388–478 636–676	WHT/ISIS	Evans/Howarth	0.5, 0.8	+1.51
2452129.6	2001.60	$\overline{3}$.61	$\overline{2}$.97	365–543 636–676	WHT/ISIS	Evans/Howarth	0.8, 0.8	+1.46
2452130.4	2001.60	$\overline{3}$.61	$\overline{2}$.97	388–478 636–676	WHT/ISIS	Evans/Howarth	0.5, 0.8	+1.49
2452132.7	2001.61	$\overline{3}$.61	$\overline{2}$.97	635–677	INT/IDS	Srv/Herrero	0.6	+1.35
2452483.6	2002.57	$\overline{2}$.27	$\overline{1}$.20	625–681	INT/IDS	Srv/Herrero	0.6	+0.39
2452508.2	2002.64	$\overline{2}$.31	$\overline{1}$.21	322–703	INT/IDS	Araujo/Gansicke	3.8	+0.79
2452528.8	2002.69	$\overline{2}$.35	$\overline{1}$.23	320–733	Bok	Wagner/Bond	1.6, 2.6	+1.19
2452549.4	2002.75	$\overline{2}$.39	$\overline{1}$.24	440–775	WHT/ISIS	Rix/Pettini	1.8–2.6	+1.34
2452566.3	2002.80	$\overline{2}$.42	$\overline{1}$.25	395–485 633–708	WHT/ISIS	Crowther	0.8	+1.42
2452607.3	2002.91	$\overline{2}$.50	$\overline{1}$.28	382–797	WHT/ISIS	Evans/Crowther	0.8, 3.0	+1.33
2452632.3	2002.98	$\overline{2}$.54	$\overline{1}$.29	405–495	WHT/ISIS	Harries	0.7	
2452775.0	2003.37	$\overline{2}$.81	$\overline{1}$.39	405–473	WIYN	Bond	0.6	
2452801.6	2003.44	$\overline{2}$.86	$\overline{1}$.40	386–684	WHT/ISIS	Lennon/Herrero	0.6–1.2	−2.70
2452803.7	2003.45	$\overline{2}$.86	$\overline{1}$.41	425–472	INT/IDS	Christian	0.3	
2452808.5	2003.46	$\overline{2}$.87	$\overline{1}$.41	380–700	WHT/ISIS	Herrero	0.7	−2.66
2452810.8	2003.47	$\overline{2}$.88	$\overline{1}$.41	405–473	WIYN	Bond	3.9	
2452816.6	2003.48	$\overline{2}$.89	$\overline{1}$.41	330–684	INT/IDS	Lennon	0.6	−2.67
2452831.6	2003.52	$\overline{2}$.91	$\overline{1}$.42	372–519 599-697	INT/IDS	Prada	0.7	−3.00
2452832.5	2003.53	$\overline{2}$.92	$\overline{1}$.42	332–498 586–705	INT/IDS	Howarth	1.4, 1.1	−3.69
2452833.4	2003.53	$\overline{2}$.92	$\overline{1}$.42	587–704	INT/IDS	Howarth	1.1	−3.92
2452834.7	2003.53	$\overline{2}$.92	$\overline{1}$.43	353–521	INT/IDS	Howarth	1.1	
2452835.7	2003.53	$\overline{2}$.92	$\overline{1}$.43	353–522 585–697	INT/IDS	Howarth	1.4, 1.1	−3.79
2452836.7	2003.54	$\overline{2}$.92	$\overline{1}$.43	352–522	INT/IDS	Howarth	1.4	
2452837.6	2003.54	$\overline{2}$.93	$\overline{1}$.43	382–490 630–683	INT/IDS	Howarth	1.1, 0.5	−3.74
2452838.6	2003.54	$\overline{2}$.93	$\overline{1}$.43	382–491 627–683	INT/IDS	Howarth	1.1, 0.5	−3.15
2452845.9	2003.56	$\overline{2}$.94	$\overline{1}$.43	405–473	WIYN	Harmer/Bond	0.6	
2452854.8	2003.59	$\overline{2}$.96	$\overline{1}$.44	405–473	WIYN	Harmer/Bond	0.6	
2452871.2	2003.63	$\overline{2}$.99	$\overline{1}$.45	391–716	OMM	Pellerin	3.9	−4.30
2452902.6	2003.72	$\overline{1}$.05	$\overline{1}$.47	405–473	WIYN	Bond	0.6	
2452913.7	2003.75	$\overline{1}$.07	$\overline{1}$.48	334–648	MMT	Bond	3.6	
2452919.3	2003.76	$\overline{1}$.08	$\overline{1}$.48	634–677	OHP/Aurelie	Rauw	0.6	−3.61
2452922.4	2003.77	$\overline{1}$.08	$\overline{1}$.48	446–490	OHP/Aurelie	Rauw	0.6	
2452980.3	2003.93	$\overline{1}$.19	$\overline{1}$.52	373–547 576–756	WHT/ISIS	Lennon/Herrero	1.2	−1.40
2453132.9	2004.35	$\overline{1}$.47	$\overline{1}$.62	444–674	OHP/Elodie	Rauw	0.3	+1.52
2453132.9	2004.35	$\overline{1}$.47	$\overline{1}$.62	405–474	WIYN	Harmer/Bond	0.6	
2453146.7	2004.39	$\overline{1}$.50	$\overline{1}$.63	374–550 568–742	WHT/ISIS	Licandro	1.6	+1.30
2453147.4	2004.39	$\overline{1}$.50	$\overline{1}$.63	371–693	Skinakas	Reig	2.0	+1.27
2453157.7	2004.42	$\overline{1}$.52	$\overline{1}$.64	359–494 604–681	WHT/ISIS	Howarth	0.8	+1.30
2453180.4	2004.48	$\overline{1}$.56	$\overline{1}$.65	550–686	Skinakas	Reig	2.0	+1.30
2453182.4	2004.48	$\overline{1}$.57	$\overline{1}$.65	375–510	Skinakas	Reig	2.0	
2453192.5	2004.51	$\overline{1}$.59	$\overline{1}$.66	390–682	OHP/Elodie	Siviero	0.1	+1.29
2453193.4	2004.51	$\overline{1}$.59	$\overline{1}$.66	551–687	Skinakas	Reig	2.0	+1.45
2453194.4	2004.52	$\overline{1}$.59	$\overline{1}$.66	377–509	Skinakas	Reig	2.0	
2453202.5	2004.54	$\overline{1}$.60	$\overline{1}$.66	350–530 609–818	Loiano	Negueruela	3.0, 3.0	+1.50
2453203.5	2004.54	$\overline{1}$.61	$\overline{1}$.66	388–999	Loiano	Negueruela	0.7	+1.47
2453209.7	2004.56	$\overline{1}$.62	$\overline{1}$.67	449–540 597–688	WHT/ISIS	R.C. Smith	0.7	+1.36
2453210.5	2004.56	$\overline{1}$.62	$\overline{1}$.67	449–540 597–689	WHT/ISIS	R.C. Smith	0.7	+1.34

JD	Year	Phase ϕ_α (Hα)	Phase φ (orb)	λ range (nm)	Telescope/ Instrument	Observer	$\Delta\lambda$ (Å)	W_λ(Hα) (Å)
2453225.8	2004.60	$\bar{1}.65$	$\bar{1}.68$	372–684	SPM	Georgiev	0.4	+1.31
2453243.4	2004.65	$\bar{1}.68$	$\bar{1}.69$	362–684	Skinakas	Reig	2.0	+1.06
2453246.3	2004.66	$\bar{1}.69$	$\bar{1}.69$	401–590 653–674	OHP/Elodie	Srv/Rauw	0.3	+1.02
2453250.5	2004.67	$\bar{1}.69$	$\bar{1}.70$	353–505 602–688	WHT/ISIS	Ostensen/Howarth	0.6	+0.89
2453251.3	2004.67	$\bar{1}.70$	$\bar{1}.70$	401–590 653–674	OHP/Elodie	Srv/Rauw	0.3	+0.89
2453252.4	2004.67	$\bar{1}.70$	$\bar{1}.70$	365–683	Skinakas	Reig	2.0	+0.90
2453261.3	2004.70	$\bar{1}.71$	$\bar{1}.70$	363–570	Skinakas	Reig	2.0	
2453262.4	2004.70	$\bar{1}.72$	$\bar{1}.70$	363–684	Skinakas	Reig	2.0	+0.73
2453264.3	2004.71	$\bar{1}.72$	$\bar{1}.70$	420–710	Crimea	Antokhin	0.5	+0.72
2453265.3	2004.71	$\bar{1}.72$	$\bar{1}.71$	420–710	Crimea	Antokhin	0.5	+0.62
2453266.3	2004.71	$\bar{1}.72$	$\bar{1}.71$	420–710	Crimea	Antokhin	0.5	+0.53
2453266.6	2004.71	$\bar{1}.72$	$\bar{1}.71$	346–505 597–689	WHT/ISIS	Benn/Howarth	0.6	+0.58
2453267.2	2004.72	$\bar{1}.72$	$\bar{1}.71$	420–710	Crimea	Antokhin	0.5	+0.58
2453267.4	2004.72	$\bar{1}.73$	$\bar{1}.71$	401–590 653–674	OHP/Elodie	Srv/Rauw	0.3	+0.60
2453269.2	2004.72	$\bar{1}.73$	$\bar{1}.71$	420–710	Crimea	Antokhin	0.5	+0.62
2453270.2	2004.72	$\bar{1}.73$	$\bar{1}.71$	420–710	Crimea	Antokhin	0.5	+0.40
2453272.4	2004.73	$\bar{1}.73$	$\bar{1}.71$	401–590 653–674	OHP/Elodie	Srv/Rauw	0.3	+0.54
2453275.2	2004.74	$\bar{1}.74$	$\bar{1}.71$	420–710	Crimea	Antokhin	0.5	+0.30
2453276.2	2004.74	$\bar{1}.74$	$\bar{1}.71$	420–710	Crimea	Antokhin	0.5	+0.18
2453278.3	2004.75	$\bar{1}.75$	$\bar{1}.71$	401–590 653–674	OHP/Elodie	Srv/Rauw	0.3	+0.25
2453282.4	2004.76	$\bar{1}.75$	$\bar{1}.72$	365–685	Skinakas	Reig	2.0	
2453282.4	2004.76	$\bar{1}.75$	$\bar{1}.72$	370–790	TNG/SARG	Andreuzzi	0.04	+0.22
2453283.3	2004.76	$\bar{1}.75$	$\bar{1}.72$	401–590 653–674	OHP/Elodie	Srv/Rauw	0.3	+0.18
2453286.4	2004.77	$\bar{1}.76$	$\bar{1}.72$	445–490	OHP/Aurelie	Rauw	0.6	
2453289.3	2004.78	$\bar{1}.77$	$\bar{1}.72$	636–675	OHP/Aurelie	Rauw	0.6	−0.27
2453290.6	2004.78	$\bar{1}.77$	$\bar{1}.72$	647–714	KPNO	Gies	0.7	−0.42
2453291.6	2004.78	$\bar{1}.77$	$\bar{1}.72$	647–714	KPNO	Gies	0.7	−0.31
2453293.3	2004.79	$\bar{1}.77$	$\bar{1}.72$	445–490	OHP/Aurelie	Rauw	0.6	
2453302.3	2004.81	$\bar{1}.79$	$\bar{1}.73$	401–590 653–674	OHP/Elodie	Srv/Rauw	0.3	−0.64
2453304.3	2004.82	$\bar{1}.79$	$\bar{1}.73$	644–662	Skinakas	Reig	2.0	−0.80
2453314.6	2004.84	$\bar{1}.81$	$\bar{1}.74$	366–668	SPM	Georgiev	0.3	−1.44
2453316.3	2004.85	$\bar{1}.82$	$\bar{1}.74$	401–590 653–674	OHP/Elodie	Srv/Rauw	0.3	−1.44
2453320.3	2004.86	$\bar{1}.82$	$\bar{1}.74$	401–590 653–674	OHP/Elodie	Srv/Rauw	0.3	−1.60
2453324.3	2004.87	$\bar{1}.83$	$\bar{1}.74$	390–682	OHP/Elodie	Srv/Rauw	0.1	−1.77
2453326.3	2004.88	$\bar{1}.83$	$\bar{1}.74$	401–590 653–674	OHP/Elodie	Srv/Rauw	0.1	−1.85
2453346.4	2004.93	$\bar{1}.87$	$\bar{1}.76$	381–703	PicMidi/Musicos	Negueruela	0.1	−3.25
2453368.3	2004.99	$\bar{1}.91$	$\bar{1}.77$	360–537 613–704	WHT/ISIS	Roeloefs/Howarth	1.1, 0.6	−3.65
2453369.3	2004.99	$\bar{1}.91$	$\bar{1}.77$	360–537 613–704	WHT/ISIS	Roeloefs/Howarth	1.1, 0.6	−3.53
2453371.3	2005.00	$\bar{1}.92$	$\bar{1}.77$	353–502 611–777	WHT/ISIS	Gaensicke	1.7, 3.2	−3.48
2453444.8	2005.20	0.06	$\bar{1}.82$	364–834	NOT/ALFOSC	Licandro	2.8	−3.90
2453446.7	2005.21	0.06	$\bar{1}.82$	639–705	Asiago	Morel	1.2	−3.53
2453458.5	2005.24	0.08	$\bar{1}.83$	637–673	Tartu	Annuk/Kolka	1.5	−3.70
2453465.6	2005.26	0.09	$\bar{1}.83$	401–590 653–674	OHP/Elodie	Srv/Rauw	0.3	−3.22
2453472.8	2005.28	0.11	$\bar{1}.84$	550–700	FMO	McDavid	1.8	−3.29
2453474.6	2005.28	0.11	$\bar{1}.84$	401–590 653–674	OHP/Elodie	Srv/Rauw	0.3	−3.01
2453480.7	2005.30	0.12	$\bar{1}.84$	350–505 600–689	WHT/ISIS	Licandro	0.6	−2.96
2453486.9	2005.32	0.13	$\bar{1}.85$	560–680	FMO	McDavid	1.8	−2.80
2453488.6	2005.32	0.14	$\bar{1}.85$	401–590 653–674	OHP/Elodie	Srv/Rauw	0.3	−2.42
2453515.4	2005.39	0.19	$\bar{1}.87$	509–716	Skinakas	Reig	2.0	−1.49
2453519.6	2005.41	0.19	$\bar{1}.87$	401–590 653–674	OHP/Elodie	Srv/Rauw	0.3	−1.08
2453536.7	2005.45	0.23	$\bar{1}.88$	401–590 653–674	OHP/Elodie	Srv/Rauw	0.3	−0.44
2453545.0	2005.48	0.24	$\bar{1}.89$	369–1048	CFHT/ESPaDOnS	Donati	0.06	
2453545.4	2005.48	0.24	$\bar{1}.89$	510–715	Skinakas	Reig	2.0	
2453546.0	2005.48	0.24	$\bar{1}.89$	369–1048	CFHT/ESPaDOnS	Donati	0.06	
2453547.0	2005.48	0.25	$\bar{1}.89$	369–1048	CFHT/ESPaDOnS	Donati	0.06	−0.14
2453548.0	2005.48	0.25	$\bar{1}.89$	369–1048	CFHT/ESPaDOnS	Donati	0.06	
2453554.6	2005.50	0.26	$\bar{1}.89$	401–590 653–674	OHP/Elodie	Srv/Rauw	0.3	+0.37
2453559.5	2005.52	0.27	$\bar{1}.90$	391–999	Loiano	Negueruela	1.5	+0.48
2453563.4	2005.53	0.28	$\bar{1}.90$	468–716	Skinakas	Reig	2.0	+0.51
2453565.5	2005.53	0.28	$\bar{1}.90$	510–716	Skinakas	Reig	2.0	+0.63
2453568.5	2005.54	0.29	$\bar{1}.90$	401–590 653–674	OHP/Elodie	Srv/Rauw	0.3	+0.66
2453585.5	2005.59	0.32	$\bar{1}.91$	390–682	OHP/Elodie	Srv/Rauw	0.1	+0.94
2453594.5	2005.61	0.33	$\bar{1}.92$	401–590 653–674	OHP/Elodie	Srv/Rauw	0.3	+1.22

JD	Year	Phase ϕ_α (Hα)	Phase φ (orb)	λ range (nm)	Telescope/ Instrument	Observer	$\Delta\lambda$ (Å)	W_λ(Hα) (Å)
2453600.3	2005.63	0.34	$\overline{1}$.92	362–715	Skinakas	Reig	2.0	+1.29
2453601.5	2005.63	0.35	$\overline{1}$.92	389–682	OHP/Elodie	Bouret/Negueruela	0.3	+1.39
2453603.9	2005.64	0.35	$\overline{1}$.92	646–662	DAO	Bohlender	0.3	+1.50
2453606.9	2005.64	0.36	$\overline{1}$.93	647–662	DAO	Bohlender	0.3	+1.37
2453607.4	2005.65	0.36	$\overline{1}$.93	648–684	Tartu	Kolka	1.5	+1.38
2453609.8	2005.65	0.36	$\overline{1}$.93	647–662	DAO	Bohlender	0.3	+1.30
2453615.4	2005.67	0.37	$\overline{1}$.93	637–673	Tartu	Kolka	1.5	+1.38
2453616.4	2005.67	0.37	$\overline{1}$.93	649–662	Tartu	Kolka	0.5	+1.54
2453620.4	2005.68	0.38	$\overline{1}$.94	649–662	Tartu	Kolka	0.5	+1.45
2453621.4	2005.68	0.38	$\overline{1}$.94	637–673	Tartu	Kolka	1.5	+1.42
2453625.4	2005.70	0.39	$\overline{1}$.94	401–590 653–674	OHP/Elodie	Srv/Rauw	0.3	+1.52
2453627.4	2005.70	0.39	$\overline{1}$.94	637–674	Tartu	Kolka	1.5	+1.49
2453630.4	2005.71	0.40	$\overline{1}$.94	649–662	Tartu	Kolka	0.5	+1.38
2453631.4	2005.71	0.40	$\overline{1}$.94	637–674	Tartu	Kolka	1.5	+1.46
2453652.3	2005.77	0.44	$\overline{1}$.96	401–590 653–674	OHP/Elodie	Srv/Rauw	0.3	+1.48
2453653.3	2005.77	0.44	$\overline{1}$.96	401–590 653–674	OHP/Elodie	Srv/Rauw	0.3	+1.55
2453653.3	2005.77	0.44	$\overline{1}$.96	649–662	Tartu	Kolka	0.5	+1.36
2453668.3	2005.81	0.47	$\overline{1}$.97	390–682	OHP/Elodie	Srv/Rauw	0.03	+1.35
2453681.3	2005.85	0.49	$\overline{1}$.97	401–590 653–674	OHP/Elodie	Srv/Rauw	0.3	+1.58
2453718.6	2005.95	0.56	0.00	647–662	DAO	Bohlender	0.3	+1.37
2453722.6	2005.96	0.57	0.00	647–662	DAO	Bohlender	0.3	+1.42
2453777.1	2006.11	0.67	0.04	648–673	DAO	Bohlender	0.3	+1.03
2453782.1	2006.12	0.68	0.04	648–662	DAO	Bohlender	0.3	+0.96
2453795.7	2006.16	0.71	0.05	649–684	Tartu	Kolka	1.5	+1.00
2453810.6	2006.20	0.74	0.06	649–684	Tartu	Kolka	1.5	+0.44
2453817.6	2006.22	0.75	0.06	637–673	Tartu	Kolka	1.5	+0.14
2453836.8	2006.27	0.78	0.08	385–707	WHT/ISIS	Lennon	0.6	−0.68
2453845.5	2006.30	0.80	0.08	637–673	Tartu	Kolka	1.5	−1.18
2453860.4	2006.34	0.83	0.09	637–673	Tartu	Kolka	1.5	−1.87
2453863.4	2006.35	0.83	0.09	637–673	Tartu	Kolka	1.5	−2.08
2453865.4	2006.35	0.84	0.09	637–673	Tartu	Kolka	1.5	−2.12
2453867.4	2006.36	0.84	0.10	637–673	Tartu	Kolka	1.5	−2.09
2453871.5	2006.37	0.85	0.10	637–673	Tartu	Kolka	1.5	−2.32
2453879.4	2006.39	0.86	0.10	637–673	Tartu	Kolka	1.5	−2.47
2453889.5	2006.42	0.88	0.11	637–673	Tartu	Kolka	1.5	−3.00
2453892.7	2006.43	0.89	0.11	386–705	WHT/ISIS	Lennon	0.4	−3.11
2453895.4	2006.44	0.89	0.11	637–673	Tartu	Kolka	1.5	−3.19
2453896.0	2006.44	0.89	0.11	369–1048	CFHT/ESPaDOnS	Donati	0.06	−3.17
2453900.4	2006.45	0.90	0.12	637–673	Tartu	Kolka	1.5	−3.15
2453941.5	2006.56	0.98	0.14	384–706	WHT/ISIS	Leisy/Lennon	0.4	−4.10
2453955.4	2006.60	1.00	0.15	637–673	Tartu	Kolka	1.5	−4.00
2453956.5	2006.60	1.01	0.15	637–673	Tartu	Kolka	1.5	−3.96
2453958.4	2006.61	1.01	0.15	637–673	Tartu	Kolka	1.5	−4.14
2453966.6	2006.63	1.03	0.16	384–706	WHT/ISIS	Leisy/Lennon	0.4	−4.07
2454002.5	2006.73	1.09	0.18	384–706	WHT/ISIS	Leisy/Lennon	0.4	−3.32